McMaster University
M. Sc. Thesis Department Physics and Astronomy

Quantum Bifurcations in a Bose-Einstein Condensate

Denise Kamp

Supervisors: Prof. Dr. Duncan O'Dell
Prof. Dr. Cliff Burgess

Date: April 29th, 2022

Contents

Acknowledgement

I would like to thank my supervisors Duncan O'Dell and Cliff Burgess for their support and patience. Much appreciation also goes to my group members Liam Farrell, Sriram Sundaram, Wyatt Kirkby, and Joshua Hainge for being very welcoming and supportive.

1. Abstract

We model an atomic Bose-Einstein condensate (BEC) near an instability, looking for universal features. Instabilities are often associated with bifurcations where the classical field theory provided here by the Gross-Pitaevskii equation predicts that two or more solutions appear or disappear. Simple examples of such a situation can be realized in a BEC in a double-well potential or in a BEC rotating in a ring trap. We analyze this problem using both Bogoliubov theory and exact diagonalization. The former describes elementary excitations which display complex frequencies near the bifurcation. We make connections to the description of bifurcations using catastrophe theory but modified to include field quantization. In the collective dynamics of the system, we encounter cusp catastrophes, which are structurally stable in two dimensions, here given by the population difference z and phase difference ϕ between two modes. Once the bifurcation arises, the system undergoes a topological phase transition, as shown in figure 1.1. Here, the phase space trajectories oscillating around a previously stable fixed point (e.g. $\langle\phi\rangle = 0$ and $\langle z\rangle = 0$) form Cassini ovals with two new stable fixed points in the foci, where $\langle z\rangle \neq 0$.

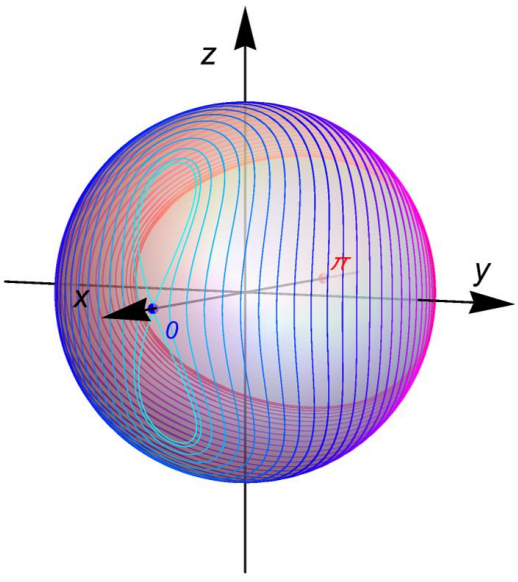

Figure 1.1.: Bloch sphere representation of the topological phase transition at the bifurcation occuring in the two-mode toroidal trap system for $\Lambda = -1$.

2. Introduction

The double-well system is a two-mode BEC trapped in a double-well potential. Each mode can either represent one of the wells or an (anti-)symmetric linear combination of both. With a tunable hopping parameter J, bosons are allowed to tunnel between the wells. There can also be an offset energy if the wells have different depths.

Similar to the double-well system, we can reduce a BEC in a slowly rotating toroidal trap to a two-mode problem. Here, the modes represent the non-rotating state and the first rotational state. Since angular momentum from the rotation is quantized, we only consider the state with the lowest angular momentum $\hbar$. Here, the modes occupy the same space, leading to additional exchange energies.

In both systems, the interaction strength U and coupling J between the modes can be tuned. At $|U| = J$ the system undergoes a phase transition, for which quasi-degeneracies in the spectrum occur. Previously stable solutions become unstable and new solutions arise. These so-called bifurcations are related to self-trapping, where bosons are trapped within one side of Fock space.

One can look at the collective dynamics of those systems in Fock space, which is the space of states of different populations in the two modes. The total number of particles is conserved, so the particle number difference between the modes is the only variable. Here, the overlap of many oscillating trajectories gives rise to so-called cusp catastrophes. Due to the nonlinearity of the system, different amplitudes of excitations have different periods, leading to those cusp-shaped lines around the focus points. Cusps are structurally stable in two dimensions, which here are given by number difference and time. Once self-trapping occurs, some cusps disappear, since some trajectories only oscillate around their initial mode, rather than exploring the entire Fock space, and don't contribute to the collective refocusing anymore.

3. Background on the Physics of Two-Mode Systems

The following chapter gives an overview of the theoretical background needed for the calculations in this thesis. We also present some experiments that realized a BEC in a ring trap. The main part of the thesis will be focusing on the toroidal trap, however, we will draw comparisons between the two systems within the two-mode approximation in the mean-field theory.

3.1. Quantum Many-Body Theory

To introduce Quantum Many-Body Theory (QMBT, second quantization), we first need to look at quantum mechanics (first quantization), in which classical observatives such as energy and momentum are elevated to operators

$$E \rightarrow \hat{H} = i\hbar\partial_t \tag{3.1}$$

$$p \rightarrow \hat{p} = -i\hbar\partial_x \tag{3.2}$$

and the Poisson bracket is replaced by the commutation relation between operators $[\hat{x}, \hat{p}] = i\hbar$. States can be represented in orthonormal bases

$$\Psi(x_1, x_2, \cdots) = \sum_n c_n \psi_n(x_1, x_2, \cdots), \tag{3.3}$$

where c_n are complex numbers. We also introduce the normalization condition

$$\int dx_1 dx_2 \cdots |\Psi(x_1, x_2, \cdots)|^2 = 1, \tag{3.4}$$

which leads to the conservation of probability. In first quantization, physical quantities are represented in terms of single-particle wavefunctions.

If we take this a little further and turn wavefunctions into field operators, we arrive at QMBT

$$\Psi(x) \rightarrow \hat{\Psi}(x) \tag{3.5}$$

with the commutation relation $[\hat{\Psi}(x_1), \hat{\Psi}^\dagger(x_2)] = \delta(x_1 - x_2)$ and the field operator $\hat{\Psi}(x)$. The field operators act on many-body states to create or annihilate particles at given position x. Depending on the choice of bases they are represented in

$$\hat{\Psi}(x) = \sum_j \hat{a}_j \psi_j(x), \tag{3.6}$$

the lowering operator $\hat{a}_j$ annihilates a particle in state j. The corresponding creation operator is $\hat{a}_j^\dagger$. The action of these operators on number states (Fock states) is given by

$$\hat{a}_j |n\rangle_j = \sqrt{n}|n-1\rangle_j \tag{3.7}$$

$$\hat{a}_j^\dagger |n\rangle_j = \sqrt{n+1}|n+1\rangle_j. \tag{3.8}$$

We also define the number operator $\hat{N} = \sum_j \hat{a}_j^\dagger \hat{a}_j = \int dx \hat{\Psi}^\dagger(x)\hat{\Psi}(x)$, which basically counts the total number of particles. QMBT allows us to investigate many-body behaviour, such as phase transitions. In QMBT the Hamiltonian generally looks like

$$\hat{H} = \int dx \hat{\Psi}^\dagger(x) \Big[-\frac{\hbar^2}{2m}\nabla^2 + V(x) \Big] \hat{\Psi}(x) + \frac{1}{2} \int dx_1 dx_2 \hat{\Psi}^\dagger(x_1)\hat{\Psi}^\dagger(x_2) U(x_1 - x_2) \hat{\Psi}(x_2)\hat{\Psi}(x_1) \tag{3.9}$$

where $V(x)$ is an external potential and $U(x_1 - x_2)$ is the two-body interaction potential, which depends on the distance between the particles. In general, more particles could be involved in the interaction, however, we only consider pairs in this thesis.

3.2. Double-Well System

We consider a double-well system with only one mode (the ground state) in each well, call them left and right modes. Technically, only eigenstates of the system are referred to as modes, however, this is only approximately true for the left and right states. Sometimes it is convenient to take the two modes as symmetric/antisymmetric linear combinations of the left and right modes, depending on the situation. With a tunable hopping parameter J, bosons are allowed to tunnel between the wells. There can also be an offset energy ϵ if the wells have different depths. The system is best described by the Hamiltonian 3.11.

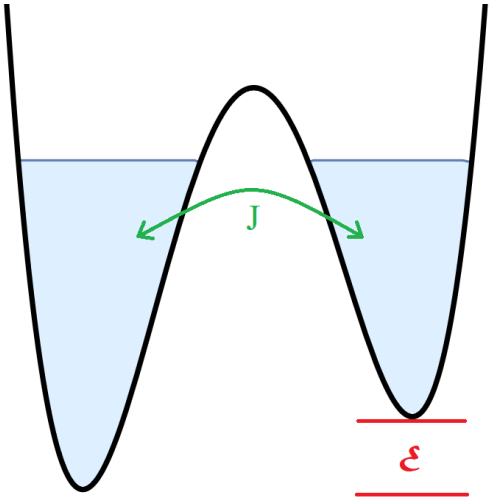

Figure 3.1.: Sketch of a double-well potential with an offset ϵ. Bosons can tunnel between wells according to hopping parameter J represented by the green line.

3.2.1. Bosonic Josephson Junction

One can use a BEC in a double-well to simulate a bosonic Josephson junction [14], where two macroscopic quantum objects are weakly coupled to each other [10]. In the absence of interactions, the ground state of the two-mode system with tunneling is given by the symmetric combination of the left and right modes, and the excited mode is given by the antisymmetric combination. The energy gap (tunneling splitting) between these two modes is $2J$. The previously introduced pair interaction is a good enough approximation in a dilute gas at low temperatures where the interaction range is much smaller than the average distance between bosons. The interaction strength for those collisions can be written as $U(x_1 - x_2) = g\delta(x_1 - x_2)$ with $g = 4\pi\hbar^2 a/m$, where a is the s-wave scattering length and m is the mass of the boson [23].

The scattering length is tunable via an experimental technique known as Feshbach resonance, and decides if interactions are attractive $(a < 0)$ or repulsive $(a > 0)$. In order for the two-mode approximation to be valid, the interaction between bosons should be weak enough that they are not excited out of the two lowest modes. This can be easily satisfied with weak enough interactions because the tunnel coupling is exponentially small, whereas the energy needed to excite the higher modes is set by the harmonic frequency of each individual well, which can be made large. Under these conditions, the Hamiltonian reads as follows

$$\hat{H} = \int dx \hat{\Psi}^\dagger(x) \Big[-\frac{\hbar^2}{2m}\nabla^2 + V(x) \Big] \hat{\Psi}(x) + \frac{g}{2} \int dx \hat{\Psi}^\dagger(x) \hat{\Psi}^\dagger(x) \hat{\Psi}(x) \hat{\Psi}(x). \tag{3.10}$$

We can write the field operators as $\hat{\Psi}(x) = \psi_g(x)\hat{b}_g^\dagger + \psi_e(x)\hat{b}_e^\dagger$. Here, $\hat{b}_g^\dagger = (\hat{b}_r^\dagger + \hat{b}_l^\dagger)/\sqrt{2}$ creates a boson in the groundstate, which is the symmetric linear combinations of the operators in the right well and left well basis [23]. For the creation operator of bosons in the excited state, we use the anti-symmetric linear combination $\hat{b}_e^\dagger = (\hat{b}_r^\dagger - \hat{b}_l^\dagger)/\sqrt{2}$. The single particle ground and excited state wavefunctions are given by $\psi_g(x) = \big[\psi_r(x) + \psi_l(x)\big]/\sqrt{2}$ and $\psi_e(x) = \big[\psi_r(x) - \psi_l(x)\big]/\sqrt{2}$. If either of those states is macroscopically occupied their time-evolution can be evaluated by looking at the Gross-Pitaevskii equation, which we will discuss in section 3.2.2.

Plugging in the new field operators in the left and right basis into the Hamiltonian 3.10 gives

$$\hat{H} = \epsilon_l N_l + \epsilon_r N_r - J\big(\hat{b}_r^\dagger \hat{b}_l + \hat{b}_l^\dagger \hat{b}_r\big) + \frac{U}{2}\big(\hat{b}_r^\dagger \hat{b}_r^\dagger \hat{b}_r \hat{b}_r + \hat{b}_l^\dagger \hat{b}_l^\dagger \hat{b}_l \hat{b}_l\big), \tag{3.11}$$

where we defined the energy levels of each well $\epsilon_{l/r}$ and the hopping parameter J over the kinetic term of the Hamiltonian 3.10, while for the interaction strength U we assume that only bosons in the same well can interact with each other. We will later use the parameters

$$\epsilon = \epsilon_r - \epsilon_l \tag{3.12}$$

$$\Lambda = \frac{UN}{2J}, \tag{3.13}$$

where ϵ gives the offset energy between the wells, and Λ is the ratio of the interaction energy UN^2 and the kinetic energy $2JN$ [14].

3.2.2. Gross-Pitaevskii Equation

The Gross-Pitaevskii equation (GPE) describes zero-temperature properties of the non-uniform BEC when scattering length is much less than the mean interparticle spacing [28]. The GPE is a non-linear Schödinger equation, where the non-linear term takes into account the mean-field produced by other bosons. Due to the non-linearity, the superposition principle does not hold for solutions of the GPE. The time-independent version takes the form

$$\left[-\frac{\hbar^2}{2m}\nabla^2 + V(x) + g|\psi(x)|^2 \right]\psi(x) = \mu\psi(x), \tag{3.14}$$

where $\psi(x)$ is a macroscopic wavefunction of the condensate treated as a classical field, which is sometimes referred to as the order parameter [28]. The eigenvalue μ is the chemical potential. The GPE is a mean-field description of the condensate. One can find the excitation energies of small fluctuations around the condensate by linearizing the GPE [17], as we will explore later in chapter 3.3.1.

3.2.3. Bogoliubov Theory

Different from the GPE, the Bogoliubov theory focuses on the microscopic theory of BECs. Here, we use creation and annihilation operators rather than working with wavefunctions. To describe a uniform system, where the momentum is a good quantum number, the Hamiltonian generally looks as follows [28], [29]

$$\hat{H} = \sum_p \frac{p^2}{2m}\hat{a}_p^\dagger \hat{a}_p + \frac{U_0}{2V}\sum_{p,p',q} \hat{a}_{p+q}^\dagger \hat{a}_{p'-q}^\dagger \hat{a}_p \hat{a}_{p'}, \tag{3.15}$$

with the volume V (not to be confused with the potential $V(x)$ above). As we investigate small quantum fluctiations around classical solutions, we use the Bogoliubov prescription, where all condensate operators are replaced by $\hat{a}_0 \to \sqrt{N_0}\exp(i\phi)$, leaving only excitation operators.

$$\hat{H} = \sum_{p\neq 0} \underbrace{\left(\frac{p^2}{2m} + U_0\frac{N_0}{V}\right)}_{\epsilon_0} \hat{a}_p^\dagger \hat{a}_p + \underbrace{U_0\frac{N_0}{V}}_{\epsilon_1}\frac{1}{2}\sum_{p\neq 0}\left(\hat{a}_p^\dagger \hat{a}_{-p}^\dagger + \hat{a}_p \hat{a}_{-p}\right) + \underbrace{\frac{N_0^2 U_0}{2V}}_{E_0}, \tag{3.16}$$

where we define $\epsilon_{0/1}$ (not to be confused with the tilt) for brevity and the condensate energy E_0, where $N_0 \approx N$. The goal is to diagonalize the Hamiltonian. The first term is already diagonal,

however, the second term is not (sometimes referred to as the squeezing operator). To fix that, we perform a canonical transformation, for which introduce a new set of operators $\hat{b}_p^\dagger$ and $\hat{b}_p$ [7],[29] as follows

$$\hat{a}_p = u_p \hat{b}_p + v_{-p}^* \hat{b}_{-p}^\dagger \tag{3.17}$$

$$\hat{a}_p^\dagger = u_p^* \hat{b}_p^\dagger + v_{-p} \hat{b}_{-p}. \tag{3.18}$$

We will use the coefficients u_p and v_{-p} to ensure a diagonal Hamiltonian. They must satisfy $|u_p|^2 - |v_{-p}|^2 = 1$, in order for the commutation relation $[\hat{b}_p, \hat{b}_{p'}^\dagger] = \delta_{p,p'}$ to hold [29]. This is in fact true for the parametrization $u_p = \cosh(\alpha_p)$ and $v_{-p} = \sinh(\alpha_p)$. If their phases are arbitrary, we can assume them to be real [28]. Due to momentum conservation, only particles of p and $-p$ are coupled by the interactions, so the whole Hamiltonian reduces to the block diagonal form

$$\begin{aligned}\hat{H} =& \left[\epsilon_0(u_p^2 + v_{-p}^2) - 2u_p v_{-p}\epsilon_1\right]\left(\hat{b}_p^\dagger \hat{b}_p + \hat{b}_{-p}^\dagger \hat{b}_{-p}\right) + E_0 \\ &+ \underbrace{\left[\epsilon_1(u_p^2 + v_{-p}^2) - 2u_p v_{-p}\epsilon_0\right]}_{=0}\left(\hat{b}_p \hat{b}_{-p} + \hat{b}_p^\dagger \hat{b}_{-p}^\dagger\right).\end{aligned} \tag{3.19}$$

To digaonalize the Hamiltonian, we must get rid of the last term. Setting the prefactor to zero, considering the parametrization of u_p and v_{-p} gives $\tanh(2\alpha_p) = \frac{\epsilon_1}{\epsilon_0}$ and finally

$$u_p^2 = \frac{1}{2}\left(\frac{\epsilon_0}{\sqrt{\epsilon_0^2 - \epsilon_1^2}} + 1\right) \tag{3.20}$$

$$v_{-p}^2 = \frac{1}{2}\left(\frac{\epsilon_0}{\sqrt{\epsilon_0^2 - \epsilon_1^2}} - 1\right), \tag{3.21}$$

where only the positive branch of the square root can be included considering that u and v are real [28]. Using those definitions in the Hamiltonian leads to the final, diagonal form

$$\hat{H} = \underbrace{\sqrt{\epsilon_0^2 - \epsilon_1^2}}_{E_e}\left(\hat{b}_p^\dagger \hat{b}_p + \hat{b}_{-p}^\dagger \hat{b}_{-p}\right) + \underbrace{\sqrt{\epsilon_0^2 - \epsilon_1^2} - \epsilon_0 + E_0}_{E_g}, \tag{3.22}$$

where E_g is the groundstate energy and E_e the energy of excitations, which must be real for the system to be stable [19].

Another way of thinking about the Bogoliubov transformation is to consider the fact that we choose the new set of operators $\hat{b}_p^\dagger$ to be eigenoperators of the Hamiltonian, thus, $[\hat{H}, \hat{b}_p^\dagger] = E_e \hat{b}_p^\dagger$ must hold for either of them [33]. With the commutation relation $[\hat{a}_p, \hat{a}_{p'}^\dagger] = \delta_{p,p'}$ we get coupled equations, which we can write in matrix form as

$$\begin{pmatrix} \epsilon_0 & -\epsilon_1 \\ \epsilon_1 & -\epsilon_0 \end{pmatrix} \begin{pmatrix} u \\ v \end{pmatrix} = E_e \begin{pmatrix} u \\ v \end{pmatrix}, \tag{3.23}$$

whose eigenvalues are given by $E_e = \sqrt{\epsilon_0^2 - \epsilon_1^2}$, which agrees with the excitation E_e found in the diagonal Hamiltonian 3.22.

3.2.4. Fock Basis

Due to particle conservation, $N = N_l + N_r$, we can reduce the many-body states to be represented by the average population difference $n = (N_r - N_l)/2$ between the left and right well in the two-mode approximation [12]. States range from $|n = -N/2\rangle$ (all the bosons in the left well) to $|n = N/2\rangle$ (all the bosons in the right well). The Hamiltonian 3.11 can be written as the tri-diagonal matrix [25]

$$\begin{aligned} \hat{H}_{n',n} =& \Big(\frac{2}{N}\Lambda n^2 + 2\epsilon n\Big)\delta_{n',n} \\ &- \Big(\sqrt{\frac{N^2}{4} + \frac{N}{2} - n(n-1)}\ \delta_{n',n-1} - \sqrt{\frac{N^2}{4} + \frac{N}{2} - n(n+1)}\ \delta_{n',n+1}\Big). \end{aligned} \tag{3.24}$$

From this Hamiltonian, we can get the generalized Raman Nath Equation, which is a Schrödinger equation in a different basis [14].

3.2.5. Schwinger Representation

We introduce operators analogous to those used in the quantum theory of angular momentum [35],[40]

$$J_x = \frac{1}{2}\left(\hat{b}_l^\dagger \hat{b}_r + \hat{b}_r^\dagger \hat{b}_l\right) = \frac{J_+ + J_-}{2} \tag{3.25}$$

$$J_y = \frac{1}{2i}\left(\hat{b}_l^\dagger \hat{b}_r - \hat{b}_r^\dagger \hat{b}_l\right) \tag{3.26}$$

$$J_z = \frac{1}{2}\left(\hat{b}_l^\dagger \hat{b}_l + \hat{b}_r^\dagger \hat{b}_r\right) = \hat{n}. \tag{3.27}$$

Thus, the hamiltonian can be written as

$$H = \frac{U}{2} J_z^2 - 2J J_x + \epsilon J_z. \tag{3.28}$$

3.2.6. Single-Particle Density Matrix

When looking at the dynamics of a system, it is convenient to have a tool to locate the condensate over time [41]. One way to predict that is to calculate and diagonalize the Single-Particle Density Matrix (SPDM) [29], which is defined as

$$\rho(x, x') = \langle \hat{\Psi}^\dagger(x) \hat{\Psi}(x') \rangle, \tag{3.29}$$

where $\hat{\Psi}^\dagger(x)$ is a field operator creating a particle at position x and the average is taken over a quantum many body state in a Fock state basis $|\Phi\rangle = \sum_{n=-N/2}^{N/2} c_n |n\rangle$ (similar to 3.3).
In the two-mode approximation with the left and right modes we can write

$$\rho(x, x') = \begin{pmatrix} \phi_l^*(x) & \phi_r^*(x) \end{pmatrix} \mathcal{M}_{SPDM} \begin{pmatrix} \phi_l(x') \\ \phi_r(x') \end{pmatrix}, \tag{3.30}$$

where the 2×2 single particle density matrix $\mathcal{M}_{SPDM}$ reads as

$$\mathcal{M}_{SPDM} = \begin{pmatrix} \sum_n \left(\frac{N}{2} + n\right) \ |c_n|^2 & \sum_n \sqrt{\frac{N}{2} + n + 1}\sqrt{\frac{N}{2} - n} \ (c^*_{n+1} c_n) \\ \sum_n \sqrt{\frac{N}{2} - n + 1}\sqrt{\frac{N}{2} + n} \ (c^*_{n-1} c_n) & \sum_n \left(\frac{N}{2} - n\right) \ |c_n|^2 \end{pmatrix}. \tag{3.31}$$

When diagonalizing the SPDM, we get two eigenvectors and their associated eigenvalues. The two-dimensional complex-valued eigenvectors Ψ_+ and Ψ_- give the natural orbitals, which are linear combinations of the two original modes, here left and right. Since the SPDM is hermitian, the eigenvalues N_+ and N_- are real and give the populations of the corresponding eigenstates [29]. If one eigenvalue is much larger than the other, the corresponding eigenstate is macroscopically occupied, which is associated with the condensate. If the eigenvalues are similar, the condensate is fragmented [25]. Both the eigenvectors and the eigenvalues can evolve over time starting from an initial state, however, they always fulfill the following constraints

$$N_+ + N_- = N_{total} \tag{3.32}$$

$$|\Psi_\pm|^2 = 1. \tag{3.33}$$

Later, we will use different choices of initial states: Fock state, Coherent state, Pegg Barnett state, and the eigenstate of the Hamiltonian. All of them will be presented in chapter 5, where we discuss the dynamics of a BEC in a slowly rotating ring trap.

3.2.7. Mean-Field Theory

When we assume the system is in a pure condensate, we can replace the operators in the Hamiltonian 3.11 with complex numbers $\hat{b}_{l/r} = \sqrt{N_{l/r}} \exp(i\phi_{l/r})$. Remeber the parameter ϵ 3.12 and Λ 3.13 and define the relative population difference z and the phase difference ϕ

$$z \equiv \frac{N_r - N_l}{N} \tag{3.34}$$

$$\phi \equiv \phi_r - \phi_l, \tag{3.35}$$

where also conservation of total particles $N = N_r + N_l$ must hold [23].

Plugging all of that in the Hamiltonian 3.11 leads to the mean-field Hamiltonian [22]

$$H_{MF} = \lim_{N\to\infty} \frac{H}{NJ} = \frac{\Lambda}{2}\, z^2 - \sqrt{1-z^2}\cos(\phi) + \epsilon z. \tag{3.36}$$

The Hamiltonian 3.36 suggests that, if we identify z with the angular momentum and ϕ with the angular displacement, the system can be interpreted as a non-rigid pendulum of momentum of inertia Λ^{-1}, where the length depends on the angular momentum [37]. Therefore, the many-body system can be described by a non-linear single particle, which is more accurate if all bosons occupy the same state.

3.2.8. Hamilton's Equations

Generally, Hamilton's equations of motion are the derivatives of the Hamiltonian with respect to the canonical coordinates z and ϕ as follows

$$\dot{z} = -\frac{\partial \tilde{\mathcal{H}}}{\partial \phi} \tag{3.37}$$

$$\dot{\phi} = \frac{\partial \tilde{\mathcal{H}}}{\partial z}. \tag{3.38}$$

Applying this to the Hamiltonian 3.36 leads to the following equations of motion

$$\dot{\phi} = \Lambda z + \frac{z}{\sqrt{1-z^2}}\cos(\phi) + \epsilon \tag{3.39}$$

$$\dot{z} = -\sqrt{1-z^2}\sin(\phi), \tag{3.40}$$

which are the Josephson equations for this system [31]. For the case $z = \pm 1$ (all bosons in one well), equation 3.39 has a singularity. To find stationary points, the equations of motion must satisfy $\dot{\phi} = \dot{z} = 0$. For equation 3.40 this is rather easy to achieve, by simply choosing $\phi_0 = 0$ or π, [44]. In the pendulum analogy, the point $\phi_0 = 0$ corresponds to a pendulum hanging straight down, while $\phi_0 = \pi$ would be a pendulum standing upright. For either choice, we can then solve equation 3.40 to find its roots $z_0(\epsilon, \Lambda)$. These solutions are shown in figure 3.2 as a function of Λ and display the characteristic shape of a pitchfork bifurcation where a single stable solution becomes unstable and at the same time two new stable solutions appear. In the presence of a tilt, the left/right symmetry of the double-well potential is broken and we obtain a broken pitchfork.

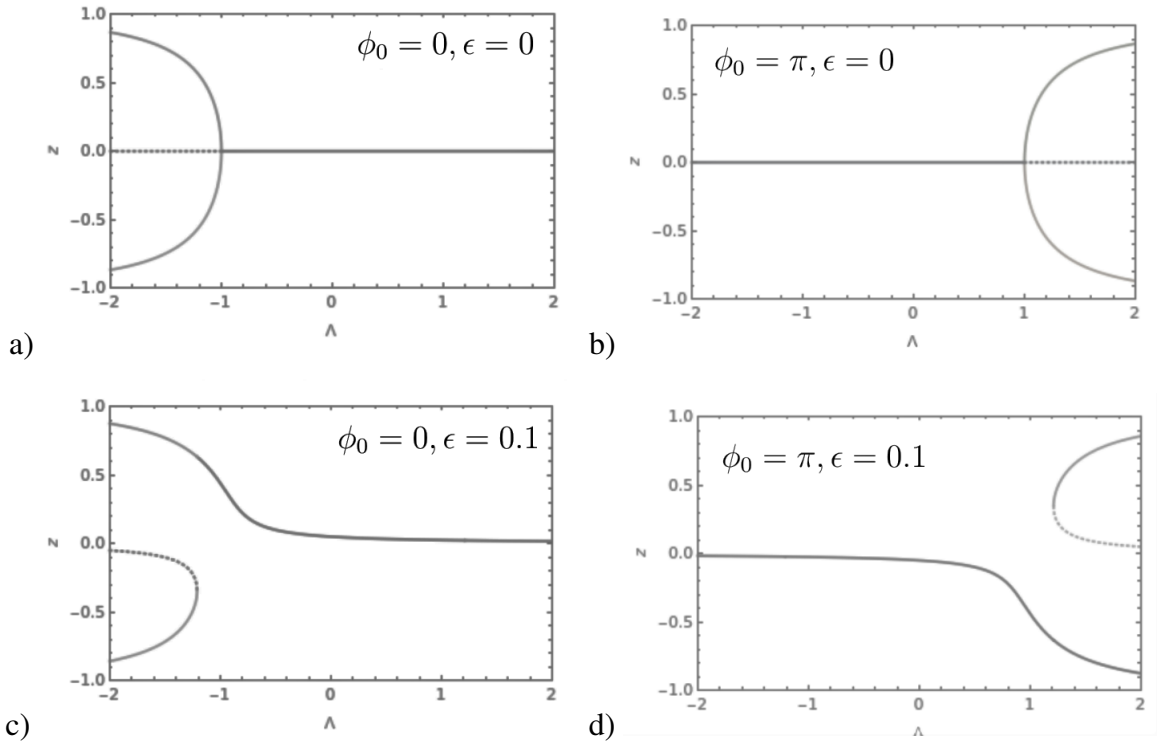

Figure 3.2.: Stationary solutions $z_0(\epsilon, \Lambda)$ of the equations of motions in dependence of Λ for a fixed tilt (upper row: $\epsilon = 0$, lower row: $\epsilon = 0.1$) result in a bifurication picture, where multiple solutions appear/disappear. The choice of ϕ_0 (left: $\phi_0 = 0$, right: $\phi_0 = \pi$) determines the orientation of the pitchfork. The dashed lines represent the unstable solutions according to figure 3.4.

Once we calculate $z_0(\epsilon, \Lambda)$ for given $\phi_0 = 0, \pi$, we can plug those back into the Hamiltonian 3.36 to find the energy of the stationary points in dependence of Λ and ϵ, as shown in figure 3.3.

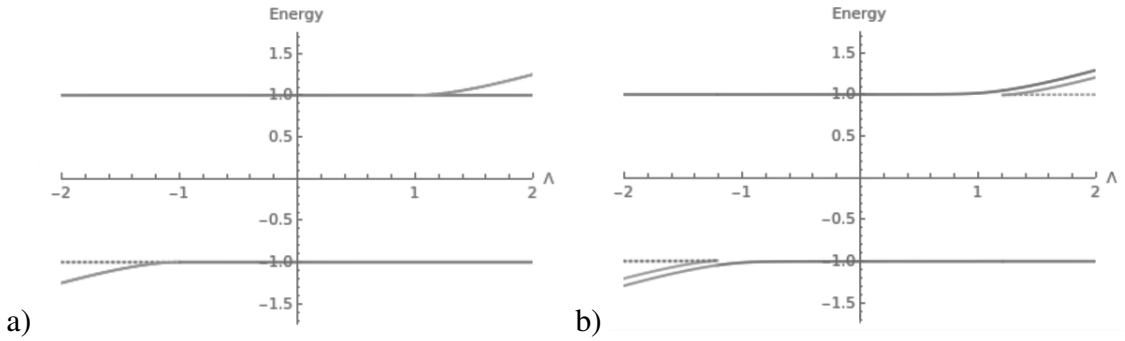

Figure 3.3.: Energy of the system, using stationary solutions $z_0(\epsilon, \Lambda)$ with $\phi_0 = \pi$ (postitve energies) and $\phi_0 = 0$ (negative energies) for different values of Λ with a) no tilt and b) $\epsilon = 0.1$. The dashed lines represent unstable solutions according to figure 3.4.

3.2.9. Stability Analysis

In general, we distinguish between two types of instabilities. There are dynamical instabilities for excitations with complex energies, such that their amplitudes grow or decay exponentially [43], causing a singularity; and then there are energetic instabilities, for excitations with negative energies [19], giving the system a tool to lower its energy by exciting particles out of the condensate.

Now, we are interested in investigating the stability of the stationary points [36]. Therefore, we perfom a linear stability analysis, for which we diagonalize the Hessian matrix 3.45 of the Hamiltonian 3.36 using the stationary solutions $\phi_0 = 0, \pi$ and $z_0(\epsilon, \Lambda) = z_0$ (for brevity). First, we introduce the following ansatz for the time dependence of z_0 and ϕ_0 with small pertubations $\delta z \propto \exp(i\omega t)$ and $\delta\phi \propto \exp(i\omega t)$

$$\phi(t) = \phi_0 + \delta\phi \rightarrow \dot{\phi} = i\omega\delta\phi \tag{3.41}$$

$$z(t) = z_0 + \delta z \rightarrow \dot{z} = i\omega\delta z. \tag{3.42}$$

The fluctuations are reduced to harmonic oscillators with the frequency ω. Performing a Taylor expansion of the Josephsons equations around the roots in the form of $f(z_0 + \delta z, \phi_0 + \delta\phi) = \underbrace{f(z_0, \phi_0)}_{=0} + \frac{\partial f(z_0,\phi_0)}{\partial z}\delta z + \frac{\partial f(z_0,\phi_0)}{\partial \phi}\delta\phi$ leads to the following expressions, where the tilt ϵ from

equation 3.39 vanishes due to the second derivatives

$$\dot{\phi}(z_0+\delta z,\phi_0+\delta\phi)=\left(\Lambda+\frac{1}{(1-z_0^2)^{\frac{3}{2}}}\cos(\phi_0)\right)\delta z-\frac{z_0}{\sqrt{1-z_0^2}}\sin(\phi_0)\delta\phi \tag{3.43}$$

$$\dot{z}(z_0+\delta z,\phi_0+\delta\phi)=-\frac{z_0}{\sqrt{1-z_0^2}}\sin(\phi_0)\delta z-\sqrt{1-z_0^2}\cos(\phi_0)\delta\phi, \tag{3.44}$$

summarized in the following matrix, which is the Hessian of the Hamiltonian 3.36

$$i\omega\begin{pmatrix}\delta\phi\\ \delta z\end{pmatrix}=\begin{pmatrix}-\frac{z_0}{\sqrt{1-z_0^2}}\sin(\phi_0) & \Lambda+(1-z_0^2)^{-\frac{3}{2}}\cos(\phi_0)\\ -\sqrt{1-z_0^2}\cos(\phi_0) & -\frac{z_0}{\sqrt{1-z_0^2}}\sin(\phi_0)\end{pmatrix}\begin{pmatrix}\delta\phi\\ \delta z\end{pmatrix}. \tag{3.45}$$

For both $\phi_0\in\{0,\pi\}$ the diagonal terms vanish since $\sin(\phi_0)=0$. Finding the eigenvalues of the Hessian Matrix 3.45 leads to

$$\omega=\sqrt{(1-z_0^2)^{\frac{1}{2}}\cos(\phi_0)\left(\Lambda+(1-z_0^2)^{-\frac{3}{2}}\cos(\phi_0)\right)}, \tag{3.46}$$

where we need to remember that $z_0=z_0(\epsilon,\Lambda)$. Therefore, the tilt influences the solutions through the root of the Josephson equation. For real frequencies ω, we find a stable oscillation, whereas, for imaginary frequencies, the fluctuations $\propto\exp(i\omega t)$ grow or decay exponentially. The frequencies 3.46 dependent on Λ are displayed in figure 3.4 compared to the corresponding bifurcation pictures from 3.2. Here, it is obvious that the stable solution for $|\Lambda|<1$ becomes unstable as soon as the two branches occur at $|\Lambda|=1$. The tilt ϵ shifts the emergence of the two new branches slightly away from $|\Lambda|=1$.

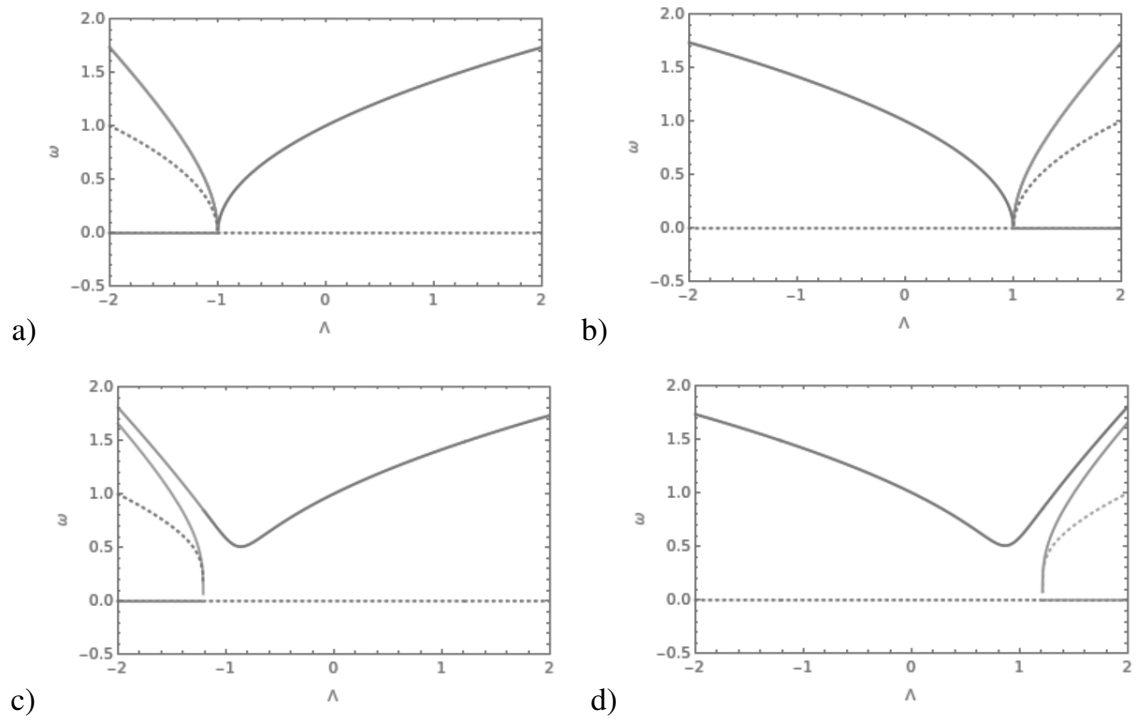

Figure 3.4.: The frequencies from equation 3.46 can be real (solid lines) or imaginary (dashed lines) for different values of Λ. The emergence of multiple frequencies at $|\Lambda| = 1$ stem from the emergence of new roots $z_0(\epsilon, \Lambda)$ displayed in figure 3.2. Here, we see the frequencies ω for a fixed tilt (upper row: $\epsilon = 0$, lower row: $\epsilon = 0.1$) for different choices of ϕ_0 (left: $\phi_0 = 0$, right: $\phi_0 = \pi$).

3.3. Toroidal Trap System

Similar to the double-well system, we can reduce a BEC in a toroidal trap to a two-mode problem. Here, the modes represent the non-rotating state and the first rotational state. Since angular momentum from the rotation is quantized [1], we only consider the states with the lowest angular momenta zero and $\hbar$. One difference compared to the double-well system is that the two modes of the toroidal trap occupy the same space [11]. This leads to an additional exchange energy term E_{ex} in the Hamiltonian 3.47.
In a toroidal trap, the condensate is located within an annulus, shown in figure 3.5. Experimental realizations are further discussed in chapter 3.5. The BEC within the trap can be rotated, which mathematically can be represented by a periodic disorder potential.

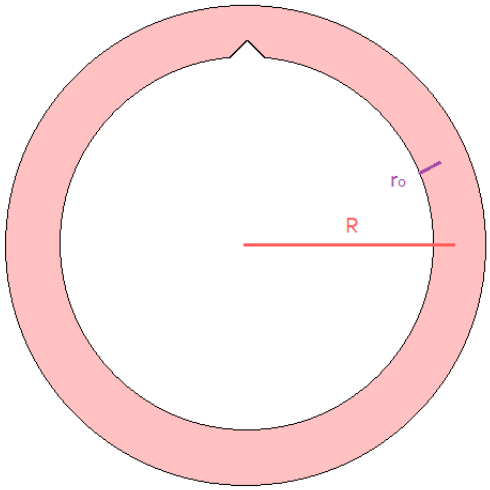

Figure 3.5.: Sketch of a toroidal trap with total radius R and cross-sectional radius of the annulus r_0. The notch on the top represents the later discussed disorder potential stirring the condensate (pink), otherwise a superfluid would not feel the rotation of a perfectly smooth trap.

3.3.1. Two-Mode Approximation and Motivation

As previously stated, we will focus on the two-mode approximation in our calculation, for which the Hamiltonian takes the Nozières form [2]

$$\mathcal{H} = \frac{\hbar^2}{2mR^2} N_1 \; + \frac{g}{2V}\Big(N_0^2 + N_1^2 + \underbrace{4N_0N_1}_{E_{ex}}\Big), \tag{3.47}$$

where m is the mass of the particle, R is the radius of the thin annulus, $V = 2\pi^2 r_0^2 R$ is the volume of the annulus with the cross-sectional radius $r_0 \ll R$ and g is the contact interaction strength. N_0 is the number of particles in the non-rotating state $|0\rangle$, while N_1 denotes the number of particles in the state $|1\rangle$ with the azimuthal angular momentum $\hbar$ per particle. The total number of particles is $N = N_0 + N_1$ and the state with $N = N_0$ is referred to as the groundstate, while $N = N_1$ is the single-vortex state. The exchange energy term E_{ex} in 3.47 gives an additional $2N_0N_1$ term, also referred to as Fock term [11], compared to $(N_0 + N_1)^2 = N^2$, which is called Hartree term [11], leading to an energy barrier between the groundstate and the single-vortex state [11], when $gN/V > \hbar^2/2mR^2$ (blue curve in figure 3.6). Weakening the interaction strength g even further leads to a decrease of the barrier until it vanishes for $gN/V \ll \hbar^2/2mR^2$, as shown in figure 3.6. Note that the interaction can still be repulsive for this to occur.

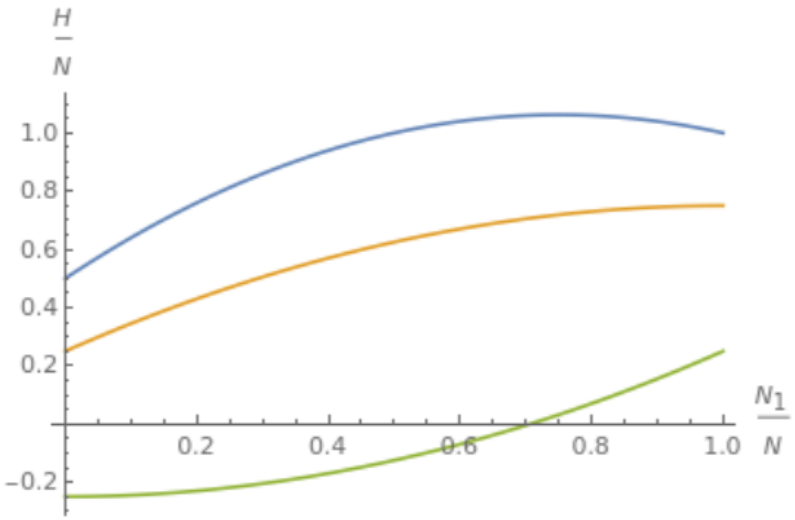

Figure 3.6.: Energy landscape of the two-level model as a function of N_1. For $gN/V > \hbar^2/2mR^2$ (blue line), there is an energy barrier between the groundstate and the single-vortex state. For $gN/V = \hbar^2/2mR^2$ (orange line), the slope vanishes at $N_1 = N$. For $gN/V \ll \hbar^2/2mR^2$ (green line) there is no energy barrier indicating the instability of the single-vortex state, especially in the attractive regime. Reproduced plot from [2].

From figure 3.6, we can see that for a condensate located on the green line in the single-vortex state (all the way to the right of the plot) it would cost no energy to relocate to the groundstate (all the way to the left). All the system needs is to find a way to lower its energy. Here, excitations with negative energies (energetically unstable) give the single vortex BEC a way of lowering its energy. In the following, we investigate how such excitations arise in this system.

3.3.2. Second Quantized Hamiltonian in Different Frames

To represent the system of a BEC in a rotating toroidal trap, we can write the Hamiltonian in terms of the operators $a_j^\dagger$ and a_j, which create and annihilate a particle with momentum $\hbar j$. However, we also have to make a choice in which frame we work [2].

First up, there is the *laboratory frame* Hamiltonian

$$\mathcal{H}_{lab} = \sum_j \frac{(\hbar j)^2}{2mR^2} a_j^\dagger a_j + \frac{g}{2V} \sum_{j,k,m} (a_{j-m}^\dagger a_{k+m}^\dagger a_k a_j), \tag{3.48}$$

where $g = \frac{4\pi\hbar a}{m}$ is the two-body interaction strength mentioned earlier and $V = 2\pi^2 r_0^2 R$ is the volume of the annulus. In this frame, the condensate Ψ_c is a solution to the time-dependent GPE.

In the *rotating frame*, the Hamiltonian $\mathcal{H}_{lab}$ is shifted by the angular velocity Ω of the trap in units of $\Omega_0 = \frac{\hbar}{mR^2}$. Obviously for $\Omega = 0$ both frames are equal.

$$\mathcal{H}_{rot} = -N\frac{\hbar\Omega^2}{2\Omega_0} + \frac{\hbar\Omega_0}{2} \sum_j \left(j - \frac{\Omega}{\Omega_0}\right)^2 a_j^\dagger a_j + \frac{g}{2V} \sum_{j,k,m} (a_{j-m}^\dagger a_{k+m}^\dagger a_k a_j). \tag{3.49}$$

In the following, we want to restrict the system to the two-mode approximation.

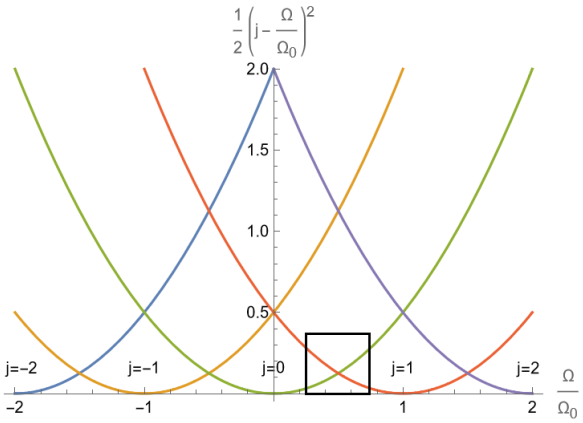

Figure 3.7.: Single particle energy level in the rotation frame from Hamiltonian 3.49 depending on the angular velocity Ω. The two-mode restriction is indicated by the black square. Reproduced plot from [2].

Thus, looking at figure 3.3.2 helps us to estimate the interval of Ω for which only the non-rotating mode (green, $j = 0$) and the first rotating mode (red, $j = 1$) are involved on a small energy scale (black square). We estimate that regime to be around

$$0.25\Omega_0 \lesssim \Omega \lesssim 0.75\Omega_0. \tag{3.50}$$

Applying the two-mode approximation to Hamiltonian 3.48 leads directly to the Hamiltonian in Nozières form 3.47, however, this breaks angular momentum conservation since the $j = -1$ mode is not considered.

3.3.3. Linearized GPE

From the GPE in the laboratory frame

$$i\hbar\partial_t\Psi_c(\theta,t) = \Big[-\frac{\hbar^2}{2mR^2}\frac{\partial^2}{\partial\theta^2} + \frac{g}{\pi r_0^2}|\Psi_c(\theta,t)|^2\Big]\Psi_c(\theta,t) \tag{3.51}$$

we get the stationary solution $\Psi_c(\theta,t) = e^{i(\theta j_c - \mu t/\hbar)}/\sqrt{2\pi R}$ representing the condensate with the chemical potential

$$\mu = \frac{j_c^2}{2} + \eta N_c, \tag{3.52}$$

where we introduced the dimensionless parameter $\eta \equiv mRg/2\pi^2\hbar^2 r_0^2 = 2aR/\pi r_0^2$ representing the interaction strength [2]. From now on, we measure angular momentum in units of $\hbar$, time in units of Ω_0^{-1} and energies in units of $\hbar\Omega_0$ and introduce another dimensionless parameter $\overline{\Omega} \equiv \Omega/\Omega_0$. We focus on the case with a condensate of N_c atoms in the single-vortex state $|1\rangle$, for which $j_c = 1$ and therefore $\mu = \frac{1}{2} + \eta N_c$, since that was the motivation from figure 3.6.
Now, we want to determine the stability of the condensate by constructing normal modes of the BEC by perturbation around the stationary solution [2], [17],[21] as follows

$$\Psi(\theta,t) = e^{-i\mu t/\hbar}\Big[\Psi_c(\theta) + \underbrace{e^{iS(\theta)}\sum_{\nu\neq 0}\Big(u_\nu\varphi_\nu(\theta)e^{-i\epsilon_\nu t/\hbar} - v_\nu^\star\varphi_\nu^\star(\theta)e^{i\epsilon_\nu t/\hbar}\Big)}_{\delta\Psi(\theta,t)}\Big] \tag{3.53}$$

with the angular momentum ν relative to the condensate, the eigenenergies ϵ_ν, the eigenstates $\varphi_\nu(\theta) = e^{i\nu\theta}\sqrt{N_c/2\pi R}$, the complex numbers u_ν ans v_ν and $S(\theta)$ the phase of $\Psi_c(\theta)$ [2].

Here, we do not apply the two-mode approximation and any $\pm\nu$ modes around the condensate are considered. Plugging the perturbation 3.53 into the GPE 3.51 leads to coupled equations that can be written as the following matrix

$$\epsilon_\nu \begin{pmatrix} u_\nu \\ v_\nu \end{pmatrix} = \begin{pmatrix} (j_c - \bar{\Omega})\nu + \left[\frac{1}{2}\nu^2 + \eta N_c\right] & -\eta N_c \\ \eta N_c & (j_c - \bar{\Omega})\nu - \left[\frac{1}{2}\nu^2 + \eta N_c\right] \end{pmatrix} \begin{pmatrix} u_\nu \\ v_\nu \end{pmatrix}. \tag{3.54}$$

Finding the eigenvalues of the matrix 3.54 gives the eigenenergies ϵ_ν for the excitations.

$$\epsilon_{\nu_{+,-}} = (j_c - \bar{\Omega})\nu \pm |\nu|\sqrt{\frac{1}{4}\nu^2 + \eta N_c}, \tag{3.55}$$

where $j_c = 1$ again for a BEC in the single vortex mode. In the following we only consider the eigenenergies ϵ_{ν_+} for positive norm states [2]. If those energies are complex e.g. $\frac{1}{4}\nu^2 + \eta N_c < 0$, the system is dynamical instable. Energetic instabilities occur for negative excitation energies, which figure 3.6 predicted to be found here. Figure 3.8 shows those regions of instabilites for excitations in the $\nu = -1$, non-rotating mode.

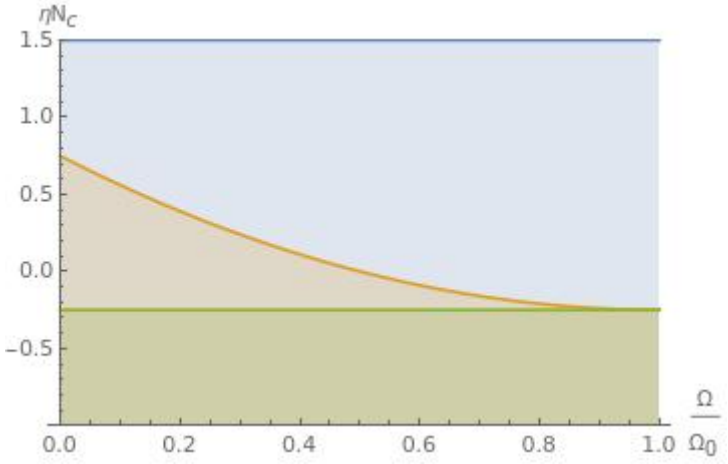

Figure 3.8.: Phase diagram for the $\nu = -1$ mode (non-rotating mode with $j = 0$) excitations in a BEC located in the single vortex state ($\nu = 0, j = 1$). The excitations are energeticly unstable (blue) for excitation energies $\epsilon_\nu < 0$ and dynamically unstability (orange) for complex ϵ_ν. Now, to ensure the two-mode approximation is valid, we must keep within the estimated interval $0.25\Omega_0 \lesssim \Omega \lesssim 0.75\Omega_0$ as established in equation 3.50. Reproduced plot from [2].

3.4. Idea of Catastrophe Theory

Generally, Catastrophe Theory is part of bifurcation theory in dynamic systems, where two or more solutions appear or disappear while slowly changing the parameter of the system as we have seen in the bifurcation pictures 3.2 from the double-well system. As we know, some of those solutions turn out to be unstable. Originally, catastrophe theory was used to describe caustics in optics, which are regions of focussing with infinite intensity, basically singularities. The shapes of the caustics are structurally stable. In the table presented in 3.9 b), we state the generating functions of different catastrophe shapes with their co-dimensions[1] $K \leq 3$.

a)

b)

name	K	generating function $\Phi(\mathbf{s};\mathbf{R})$
fold	1	$s^3 + Xs$
cusp	2	$s^4 + Xs^2 + Ys$
swallowtail	3	$s^5 + Xs^3 + Ys^2 + Zs$
elliptic umbilic	3	$s_1^3 - 3s_1s_2^2 + Z(s_1^2 + s_2^2) + Ys_2 + Xs_1$
hyperbolic umbilic	3	$s_1^3 + s_2^3 + Zs_1s_2 + Ys_2 + Zs_1$

Figure 3.9.: a) Example of a cusp shaped caustic in a coffe cup[27]. b) Table of structurally stable catastrophes and their generating functions with co-dimension $K \leq 3$ [23]. R represents the control parameters and s the state variables.

Caustics have also been found in wave theory, where the consideration of a phase leads to an interference pattern with caustics where phase singularities occur. Taking it even further, one can also find quantum caustics, which occur when looking at the collective dynamics of the system in Fock space, which is the quantum mechanical Hilbert space. Even though we will not go into further detail about catastrophe theory and its mathematical description within the purpose of this thesis, we will encounter and point out the cusp catastrophes we come across when investigating the dynamics of a two-mode BEC in a toroidal trap in chapter 5.

[1] Co-dimension is defined as dimensionality of control space minus dimensionality of singularity [24].

3.5. Experimets with BECs in a Toroidal Trap

Many research groups are interested in experimentally realizing superfluids in ring traps [4],[18]. For example, at the Joint Quantum Institute the group around G. Campbell is working with so-called atom circuits [6],[26],[32],[42]. Here, they create a superfluid BEC of approximately $500,000$ sodium atoms at temperatures about $100nK$ trapped into a ring shape. This is done by using an arrangement of $1064nm$ lasers to optically trap the atoms in a toroid, which is about $40\mu m$ wide with a cross-sectional diameter of $8\mu m$. Just as for superconductors in a ring, the angular momentum of the BEC is quantized. Thus, the current in the ring can only flow at specific velocities. For the purpose of this thesis, we only focus on the lowest two angular momenta zero and $\hbar$, which correspond to a single vortex. To excite bosons from the groundstate to any excited state, hence giving them angular momentum, one can manipulate the angular velocity of the trap $\bar{\Omega}$. Here, they use an additional $532nm$ laser exerting repulsive force on the bosons as an optical paddle to stir the BEC around. Those velocities can be up to $4Hz$. Using Feshbach resonances [28], one can tune the interactions η in a BEC to be attractive or repulsive, which is equivalent to tuning $\Lambda \propto \eta$ in our calculations.

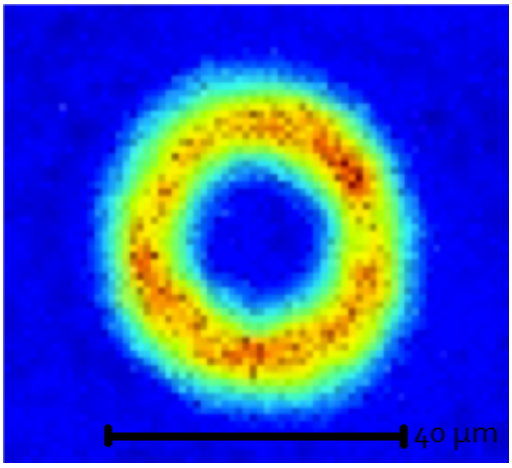

Figure 3.10.: Picture taken from G. Campbell's experiment, showing a toroidal trap with total diameter of $40\mu m$. Here, the rotation of the BEC is induced by a green laser stirring along the annulus. Picture taken from [5].

4. BEC in Toroidal Trap

Starting our calculations for a BEC in a rotating toroidal trap, we remember from chapter 3.3.1 that the Hamiltonian can be written in different frames. Previously, we discussed the laboratory frame 3.48 and the rotating frame 3.49.
However, let us also introduce the frame relative to the condensate, where we shift the angular momentum j in $\mathcal{H}_{lab} = \sum_j \frac{(\hbar j)^2}{2mR^2} a_j^\dagger a_j + \frac{g}{2V} \sum_{j,k,m} a_{j-m}^\dagger a_{k+m}^\dagger a_k a_j$ from equation 3.48 to be relative to the condensate $\nu = j - j_c$ [2], thus

$$\mathcal{H}_{rel} = \sum_\nu \frac{\hbar^2(\nu + j_c)^2}{2mR^2} a_\nu^\dagger a_\nu + \frac{g}{2V} \sum_{j,k,m} a_{j-m}^\dagger a_{k+m}^\dagger a_k a_j. \tag{4.1}$$

If the condensate is in the groundstate (non-rotating state $|0\rangle$) both frames are the same, but if the BEC is in the single vortex-state (rotating state $|1\rangle$) we know that $j_c = 1$.

4.1. Bogoliubov Transformation

As discussed in chapter 3.2.2, we can find the eigenenergies of the system by linearizing the GPE. However, from chapter 3.2.3 we also know the alternative way is to apply Bogoliubov theory [7], which we will do in the following section. For this, we will focus on the relative frame Hamiltonian 4.1, where the condensate per definition is in the $\nu = 0$ mode with the respective ladder operators $a_0^\dagger$ and a_0. Considering the BEC to be in the single-vortex state, we set the actual condensate momentum to $j_c = 1$. We will also calculate the eigenenergy in units of $\frac{\hbar^2}{mR^2}$. For brevity, we introduce the dimensionless interaction strength $\eta \equiv \frac{gmR^2}{V\hbar^2}$. For the Bogoliubov transformation, we consider excitations around the condensate, thus, we bring the Hamiltonian in a form containing only interactions, where two or four particles from the condensate are involved [1]. The Hamiltonian now reads as

[1] We do not consider the two-mode approximation here, so any $\pm\nu$ modes around the condensate are considered.

$$\mathcal{H}_{rel} = \frac{1}{2}a_0^\dagger a_0 + \frac{\eta}{2}a_0^\dagger a_0^\dagger a_0 a_0 + \sum_{\nu\neq 0}\frac{(\nu+1)^2}{2}a_\nu^\dagger a_\nu + \frac{\eta}{2}\sum_{\nu\neq 0}(4a_\nu^\dagger a_0^\dagger a_\nu a_0 + a_\nu^\dagger a_{-\nu}^\dagger a_0 a_0 + a_0^\dagger a_0^\dagger a_\nu a_{-\nu}). \tag{4.2}$$

Note that this Hamiltonian would be already diagonal for no interaction $\eta = 0$. However, in the general case of $\eta \neq 0$ we need to diagonalize the Hamiltonian in order to find the eigenenergies. We can replace the condensate operator a_0 and $a_0^\dagger \to \sqrt{N_0} \approx \sqrt{N}$ as discussed previously. However, we need to be careful this time since the condensate is not in the groundstate [9]. When replacing the operators, we have to remember the kinetic energy correction

$$E_{kin,cor} = -\frac{j_c^2}{2}\sum_\nu a_\nu^\dagger a_\nu, \tag{4.3}$$

which usually vanishes for groundstate BECs. However, we are considering the BEC to be in the first excited state $|1\rangle$ with $j_c = 1$. Also note, that this correction sum also includes the $\nu = 0$ mode, therefore, cancels out the $\frac{1}{2}a_0^\dagger a_0$ term in the front.

Additionally, we must be careful when replacing the condensate operators in the term containing four of them. For this, we have to consider the following higher-order correction term [9],[29]

$$a_0^\dagger a_0^\dagger a_0 a_0 = N^2 - 2N\sum_{\nu\neq 0}a_\nu^\dagger a_\nu. \tag{4.4}$$

Considering both of these corrections is equivalent to shifting to the grand canonical ensemble, where where $\mathcal{H}_{GC} = \mathcal{H}_{rel} - \mu\sum_\nu a_\nu^\dagger a_\nu$. After carefully replacing the condensate operators, the Hamiltonian reads

$$\mathcal{H}_{GC} = \frac{\eta}{2}N^2 + \sum_\nu\Big(\frac{(\nu+1)^2}{2}\underbrace{-\frac{1}{2}-\eta N}_{-\mu}\Big)a_\nu^\dagger a_\nu + \frac{\eta}{2}N\sum_{\nu\neq 0}(4a_\nu^\dagger a_\nu + a_\nu^\dagger a_{-\nu}^\dagger + a_\nu a_{-\nu}), \tag{4.5}$$

with the chemical potential resulting from the correction terms would be $\mu = \frac{1}{2} + \eta N$. This is equivalent to the chemical potential 3.52 found in the GPE calculations in the earlier chapter. Now, we can rearrange our Hamiltonian to look like

$$\mathcal{H}_{GC} = \frac{\eta N^2}{2} + \sum_{\nu \neq 0} \Big(\Big[\frac{\nu^2}{2} + \nu + \eta N \Big] a_\nu^\dagger a_\nu + \frac{\eta N}{2} (a_\nu a_{-\nu} + a_\nu^\dagger a_{-\nu}^\dagger) \Big). \tag{4.6}$$

Before performing the Bogoliubov Transformation it might help to shift the index of the sum from $\nu \neq 0$ to $\nu > 0$ as follows

$$\mathcal{H}_{GC} = \underbrace{\frac{\eta N^2}{2}}_{E_0} + \sum_{\nu > 0} \Big(\underbrace{\Big[\frac{\nu^2}{2} + \nu + \eta N \Big]}_{A^+} a_\nu^\dagger a_\nu + \underbrace{\Big[\frac{\nu^2}{2} - \nu + \eta N \Big]}_{A^-} a_{-\nu}^\dagger a_{-\nu} + \eta N (a_\nu a_{-\nu} + a_\nu^\dagger a_{-\nu}^\dagger) \Big), \tag{4.7}$$

to keep track of the sign of the relative angular momentum ν. Here, we defined

$$A^\pm \equiv \Big(\frac{\nu^2}{2} \pm \nu + \eta N \Big). \tag{4.8}$$

Following the Bogoliubov theory from chapter 3.2.3, we introduce the new operator $b_\gamma^\dagger$ which is a linear combination of the previous bosonic ladder operators

$$b_\gamma^\dagger = (u_\gamma a_\gamma^\dagger - v_\gamma a_{-\gamma}), \tag{4.9}$$

where γ is also angular momentum relative to the condensate and $[b_\gamma, b_\beta^\dagger] = \delta_{\gamma,\beta}$. Since $b_\gamma^\dagger$ is designed to be an eigenoperator of the Hamiltonian, $[\mathcal{H}_{GC}, b_\gamma^\dagger] = \hbar\omega_\gamma b_\gamma^\dagger$ must hold. Performing the commuator calcualtion $[\mathcal{H}_{GC}, b_\gamma^\dagger] = \mathcal{H}_{GC} b_\gamma^\dagger - b_\gamma^\dagger \mathcal{H}_{GC}$ with the Hamiltonian 4.7 and the Bogoliubov operator 4.9, we find

$$\hbar\omega_\nu b_\nu^\dagger = A^+ u_\nu a_\nu^\dagger + A^- v_\nu a_{-\nu} + \eta N u_\nu a_{-\nu} + \eta N v_\nu a_\nu^\dagger, \tag{4.10}$$

for $\nu > 0$ with $A^\pm$ defined in equation 4.8. Replacing $b_\nu^\dagger$ with equation 4.9 again, leads to the following non-hermitian eigenvalue equation

$$\begin{pmatrix} A^+ & \eta N \\ -\eta N & -A^- \end{pmatrix} \begin{pmatrix} u_\nu \\ v_\nu \end{pmatrix} = \hbar\omega_\nu \begin{pmatrix} u_\nu \\ v_\nu \end{pmatrix}. \tag{4.11}$$

Solving for the eigenvalues of this matrix leads to

$$\hbar\omega_\nu = \frac{(A^+ - A^-)}{2} \pm \sqrt{\frac{(A^+ - A^-)^2}{4} + A^+A^- - \eta^2N^2}, \tag{4.12}$$

where we can use the definition of $A^\pm$ from equation 4.8. The eigenenergies turn out to be

$$E_\nu = \nu \pm |\nu|\sqrt{\frac{\nu^2}{4} + \eta N}. \tag{4.13}$$

If we want to shift this result into the rotating frame, we simply perform a Galilean shift[8],[15] with the dimensionless angular velocity $\bar{\Omega} = \frac{\Omega}{\Omega_0}$. With that, we arrive at the expression

$$E_\nu = (1 - \bar{\Omega})\nu \pm |\nu|\sqrt{\frac{\nu^2}{4} + \eta N}, \tag{4.14}$$

which is exactly the result 3.55 we got when linearizing the GPE [2], presented in chapter 3.3.1.

4.1.1. Mapping onto Double Well

To compare the BEC in the toroidal trap to the double-well system, we need to apply the two-mode approximation. As mentioned before in chapter 3.3.1, this breaks angular momentum conservation. However, to compensate for that, we need to extend our description by including the rotation of the trap explicitly. If the trap was perfectly round and smooth, the BEC would not feel the rotation at all. Therefore, we introduce a disorder potential $\upsilon(\theta - \Omega t)$ with $\upsilon(\theta) = 2\upsilon\cos(\theta)$, where υ must be real and positive [2]. There are two ways one can visualize the physical meaning of $\upsilon(\theta)$ in the trap. First would be a periodically rotating notch (like shown in figure 3.5), making the trap less smooth and stirring the condensate. The second is a deformation of the annulus to an ellipse, like a cosine traveling along the ring. Either way, the disorder potential represents the coupling between the modes and gives a tool for the particles to change modes, much like tunneling in the double-well potential, given by the parameter J. It is completely time-independent in the rotating frame, which is why we will be starting from the Hamiltonian 3.49 in this section.
Trying to find the expectation values of this Hamiltonian $\langle\Psi|\mathcal{H}_{rot}|\Psi\rangle$, we can choose Ψ to be a coherent state. This is a convenient choice since coherent states are the eigenstate of the ladder operators, which are the only operators appearing in our Hamiltonian. Therefore, we can replace them with the complex eigenvalues $a_j \to \sqrt{N}c_j$, where $c_j \in \mathbf{C}$. In the two-mode approximation we only consider $j = 0, 1$, thus, $|c_0|^2 + |c_1|^2 = 1$ must hold. The coupling term between the condensates from the disorder potential reduces to $2N\upsilon Re(c_1^* c_0)$ and we arrive at

$$\mathcal{H} = N\Big(\frac{1}{2} - \bar{\Omega}\Big)|c_1|^2 + \frac{\eta N^2}{2}\big(1 + 2|c_0|^2|c_1|^2\big) + 2N\upsilon Re(c_1^* c_0). \tag{4.15}$$

Dividing through by $N\upsilon$ gives us the new Hamiltonian $\tilde{\mathcal{H}} = \frac{\mathcal{H}}{N\upsilon}$ as follows

$$\tilde{\mathcal{H}} = 2\epsilon|c_1|^2 + \Lambda\big(1 + 2|c_0|^2|c_1|^2\big) + 2Re(c_1^* c_0), \tag{4.16}$$

where we used the following definitions, which are the equivalents to the double-well parameters used in chapter 3.2 and function as a translation between the systems

$$\epsilon \equiv \frac{\big(\frac{1}{2} - \bar{\Omega}\big)}{2\upsilon} \qquad\qquad \Lambda \equiv \frac{\eta N}{2\upsilon}. \tag{4.17}$$

Similarly to the double-well case, we want to express the Hamiltonian in terms of a phase difference ϕ and a relative particle number difference z. To get there, we rewrite the complex numbers as $c_j = \sqrt{\frac{N_j}{N}} e^{i\phi_j}$ so that we can define[2]

$$z \equiv |c_0|^2 - |c_1|^2 \qquad\qquad \phi \equiv \phi_1 - \phi_0. \tag{4.18}$$

For the coupling term that means $Re(c_1^* c_0) \propto Re(e^{i\phi}) = \cos(\phi)$. Now, we also keep in mind that $1 = |c_0|^2 + |c_1|^2$. With all that, we arrive at

$$\tilde{\mathcal{H}} = \underbrace{\epsilon + \frac{3\Lambda}{2}}_{const.} - \epsilon z - \frac{\Lambda}{2} z^2 + \sqrt{1 - z^2}\cos(\phi). \tag{4.19}$$

Therefore, the Hamiltonian up to constant terms is exactly the negative of the double-well mean-field Hamiltonian 3.36, which can be remodeled with the following transformation

$$\Lambda \to -\Lambda \tag{4.20}$$
$$\phi \to \phi + \pi \tag{4.21}$$
$$\epsilon \to -\epsilon, \tag{4.22}$$

which, in the pendulum analogy, corresponds to a pendulum staying upright. Even without that transformation, we can get to the same equations of motions, due to the slightly different definition of ϕ, since both the Hamilton's equations 3.37 and 3.38 gain a global negative sign[3] when using the new definition of ϕ from 4.18 instead. Further details on the derivation are given in the appendix A.1. Considering the rescaling of time $\tau = 2\upsilon t$, we arrive at

$$\frac{dz}{d\tau} = -\sqrt{1 - z^2}\sin(\phi), \tag{4.23}$$
$$\frac{d\phi}{dt} = \cos(\phi)\frac{z}{\sqrt{1 - z^2}} + \Lambda z + \epsilon, \tag{4.24}$$

which agree with the equations of motion 3.39 from the double-well case.

[2]Note that the definition of ϕ is different by a negative sign from the definition 3.35 in the double-well case.
[3]For equation 3.37: $\sin(\phi) \to -\sin(\phi)$, and for equation 3.38: $\dot{\phi} \to -\dot{\phi}$.

5. Dynamics

In this chapter, we will explore the dynamics of a BEC in a toroidal trap. Here, we compare the mean-field (classical) trajectories with the quantum predictions. Since the Josephson equations 4.23 and 4.24 turned out to be the same for the toroidal trap system and the double-well system [38],[44], we expect the same phase transition to happen for the critical values $|\Lambda| = 1$, which were discussed in the bifurcation pictures 3.2 for the double well, which will be further explored in the following. Here, the universal features of the cusp catastrophe appear in the dynamics.

5.1. Mean-Field Trajectories

Using the Josephson equations of motion 4.23 and 4.24 derived in the previous chapter, we can predict the dynamics of the system after starting from a chosen initial condition z_i, ϕ_i. In classical physics, we can pick any pair of z_i, ϕ_i to watch the system evolve. However, to mimic an initial quantum state, we perform a so-called truncated Wigner approximation [13], [20],[30],[34]. We choose many different values for the phase difference ϕ_i, while picking one specific number difference z_i, which gives a pseudo-Fock state. Figure 5.3 gives a good overview of the color code used to denote the different initial phase differences. All mean-field trajectories are results from the classical equations of motion. Besides the initial condition, we can also manipulate the dimensionless interaction Λ [38] and the angular velocity of the trap $\bar{\Omega}$ [26]. For the latter, we must ensure to stay within the regime where the two-mode approximation is valid: $0.25 < \bar{\Omega} < 0.75$, as discussed in equation 3.50. We calculated the expectation value of the population difference, which is the average over all trajectories denoted by a blue curve in the plots. In Appendix A.2 we present the effect of the parameters Λ, $\bar{\Omega}$ and z_i on the dynamics. To explore the expected phase transitions for the critical values $|\Lambda| = 1$, we plot the classical trajectories in a phase diagram 5.1, which gives equivalent insight for the toroidal system as the bifurcation pictures 3.2 did for the double well system [39],[44]. Here, we pick the critical value $\Lambda_c = -1$, where the stable fixed point at $\phi = 0$ (blue point in Bloch sphere figures 5.1) becomes unstable and two new stable fixed points emerge.

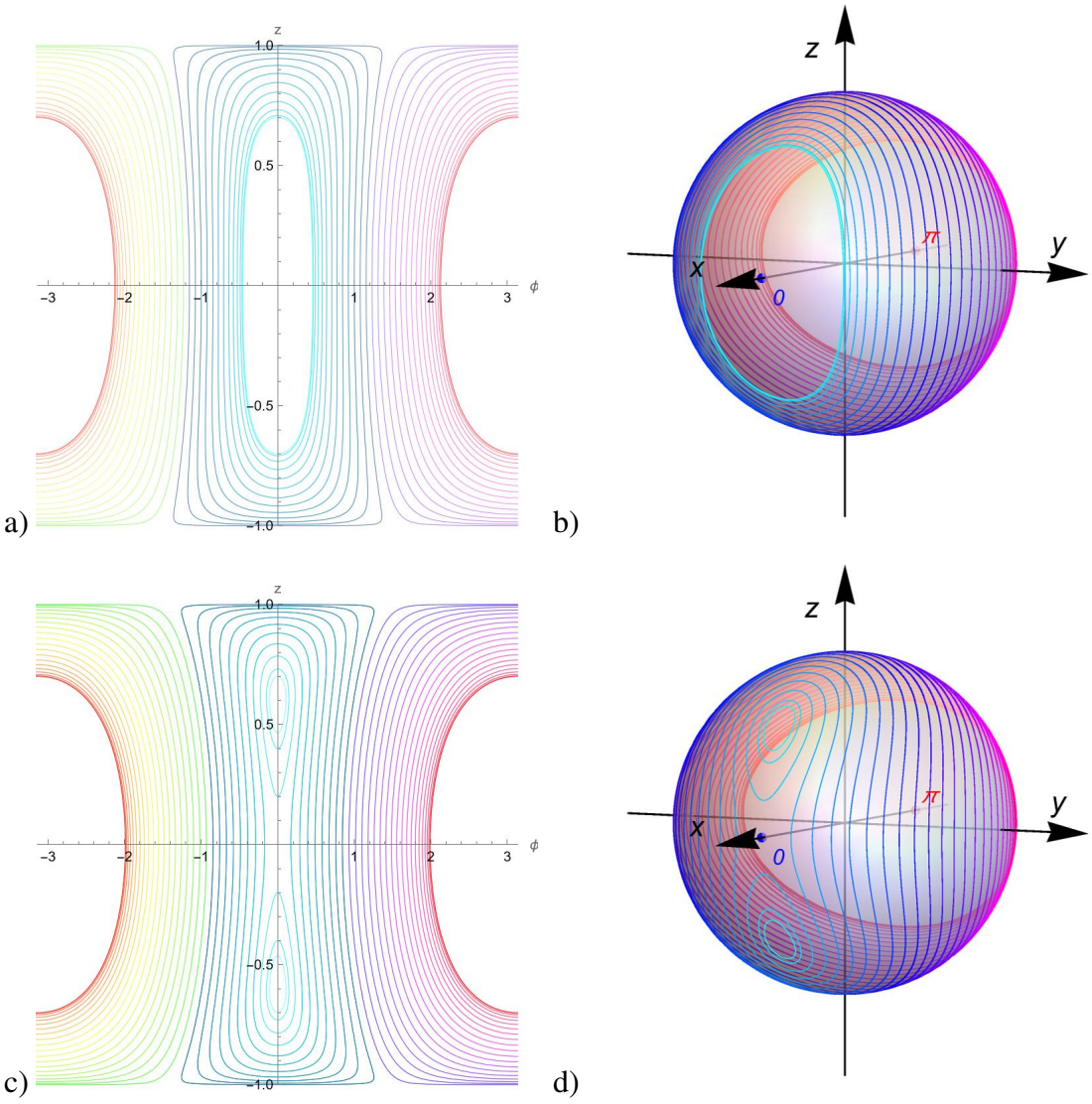

Figure 5.1.: Mean-field phase space trajcetories derived from the Josephson equation (4.23, 4.24) with $\bar{\Omega} = 0.5$ (thus $\epsilon = 0$) and $z_i = \pm 0.7$. The many initial phase differences ϕ_i are donoted by the colors, where yellow and pink trajectories form the flat phase space (left) overalp in the Bloch sphere representation (right). Here, we tune the parameter Λ from $\Lambda = -0.75$ (upper row) past the critical values $\Lambda_c = -1$, for which the stationary point $\phi = 0$ becomes unstable, to $\Lambda = -1.25$ (lower row). This reproduces the essence of the bifurcation pictures 3.2 in the double-well system.

The phase space trajectories show how the two parameters z and ϕ evolve over time, depending on their initial conditions z_i and ϕ_i. Here, we chose the same z_i for all trajectories. In the usual phase space representation in figure 5.1 (left), the different values for ϕ_i are denoted by different colours. Here, the yellow and purple trajectories connect at the edge at $\phi = \pm\pi$. Another way of representing the phase space trajectories is on a sphere, where the projection on the z-axis represents the population difference and the azimuthal angle ϕ the phase difference. The radius is set to one. Here, the previously yellow and pink trajectories overlap. We explicitly show the initially stable fixed points at $\phi = 0, \pi$ (blue and red points) and all the oscillations around them. The oscillations with $\langle\phi\rangle = \pi$ (red point) are called π-oscillations and $\langle\phi\rangle = 0$ (blue point) plasma oscillations [44]. Both representations in figure 5.1 give great insight into the behavior of the trajectories when tuning Λ past the critical value $\Lambda_c = |1|$. The sign of the critical value $\Lambda_c = \pm 1$ determines, whether plasma oscillations or π-oscillations undergo the topological phase transition, as shown in the appendix in figure A.7.

For $\Lambda > -1$, we can clearly see the elliptical shape of the plasma oscillation trajectories. They become narrower approaching the critical value, where the closest trajectory (blue line in flat phase space) breaks up into a figure eight like shape through the stationary point forming a Cassini oval, which constitutes a topological phase transition[1]. Tuning $\Lambda < -1$, some trajectories get trapped inside one loop of the figure eight and revolve around new stable fixed points $\langle z\rangle \neq 0$, which is referred to as self-trapping [44]. Note that each of the two new fixed points stems from one of the two initial conditions $z_i = \pm 0.7$. Looking at the Bloch sphere representation, those fixed points are located on opposite hemispheres. In order for both points to emerge, we need to consider both initial conditions, otherwise, the symmetry is broken. The self-trapped trajectories correspond to the stable bifurcation branches seen in the pitchfork pictures 3.2 [39]. Other trajectories still encircle the whole figure eight and all trajectories inside including the point $\phi = 0$ at $\langle z\rangle = 0$. Those correspond to the unstable solution (dashed line) in figure 3.2.
The same behavior is evident in the classical trajectories in Fock space, figure 5.2. Initially, for $\Lambda > -1$, all trajectories oscillate through the whole of Fock space with $\langle z\rangle = 0$. However, for $\Lambda < -1$, some trajectories for previously stable plasma oscillations (light blue lines in figure 5.2) are now self-trapped on one side of Fock space, oscillating around a fixed value[2] with $\langle z\rangle \neq 0$. The π-oscillations (red lines) remain the same. Considering only one initial condition $z_i = -0.7$ leads to symmetry breaking, where trajectories are self-trapped around only one of the fixed points[3].

[1] The Bloch sphere for this scenario is shown in figure 1.1 in the abstract.
[2] Corresponding to just one of the new stable fixed point in figure 3.8.
[3] Plotting all trajectories for both initial conditions at once is shown in the appendix in figure A.5 for $\Lambda > 1$.

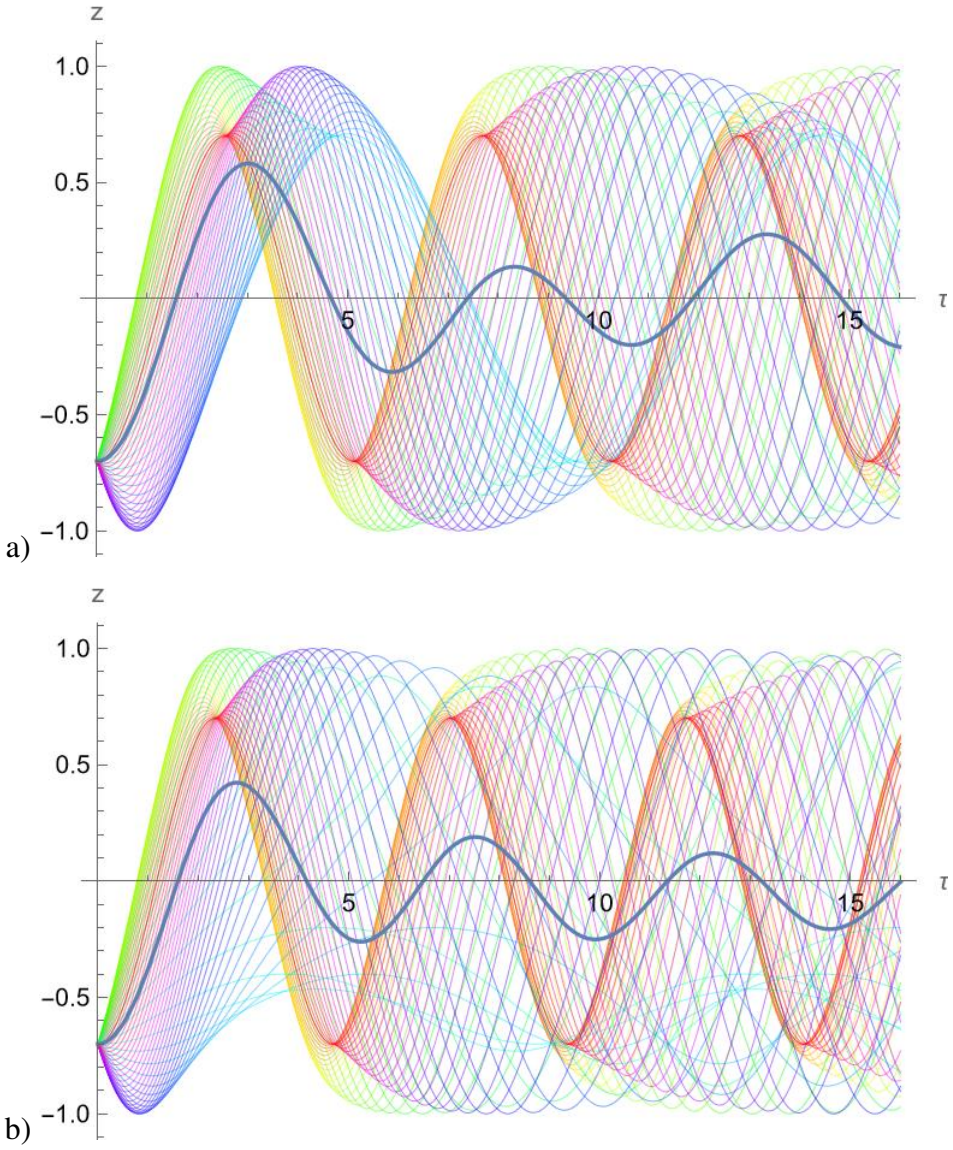

Figure 5.2.: Mean-field trajectories in Fock space from the Josephson equations (4.23, 4.24) with $\bar{\Omega} = 0.5$ (thus $\epsilon = 0$) and $z_i = -0.7$, for the many different initial phase differences ϕ_i, denoted by the colors. Here, we tune the parameter Λ from a) $\Lambda = -0.75$ past the critical values $\Lambda_c = -1$, for which the stationary point $\phi = 0$ becomes unstable, to b) $\Lambda = -1.25$. Some trajectories with $\phi_i \approx 0$ (light blue) are self-trapped on one side of Fock space due to the bifurcation effect shown is 5.1

Looking at the Fock space trajectories 5.2, we can clearly see that some of them refocus throughout the time evolution. For different amplitudes ϕ_i, the oscillation is faster or slower causing the trajectory to overshoot or miss the focus point. This leads to the appearance of cusp shapes, as introduced in chapter 3.4. In the case of $\Lambda > -1$, before the bifurcation, two types[4] of cusps appear with different orientations. For π-oscillations (red lines in figure 5.2), cusps emerge from the focus point facing forward, whereas, for plasma oscillations (blue lines), the cusps are facing backward, eventuating in a focus point[5]. Once Λ passes the critical value, the backward-facing cusps vanish due to the self-trapping. Considering the time-evolution of the phase difference ϕ in phase space 5.3 gives further insight into the behavior of the system when undergoing the phase transition. Here, for either choice of Λ, the π-osciallations (red lines) clearly revolve around $\langle\phi\rangle = \pi$ and the plasma oscillations (light blue lines) around $\langle\phi\rangle = 0$. The Cassini oval shape of the trajectories in figure 5.1 causes the phase space trajectories for the plasma oscillations to be rather flat. Since the trajectories of π-oscillations approach a circle shape, their phase space representation takes a more familiar sine function form. It is evident that once $\Lambda < -1$, some of the plasma oscillations (light blue lines) stay closer to their initial value as they become self-trapped around the new stable fixed points, which are the foci of the Cassini oval. If we considered the other critical point $\Lambda = 1$, where the π-oscillations become unstable, the red lines would stay closer to their initial values due to self-trapping, as shown in figure A.4. If $\Lambda \gg |1|$, all trajectories will be self-trapped around one of the stable fixed points. Now, we remember that $\Lambda \propto \eta/\upsilon$ (from equation 4.17), where η is the interaction strength and υ the coupling parameter between the modes (much like U and J in the double-well system, respectively). Very large magnitudes of Λ correspond to a very small coupling between the modes. Therefore, bosons are less likely to switch modes, such that they mostly remain in their initial modes. Hence, the population difference varies only slightly, keeping most of the trajectories on one side of Fock space, as shown in figure A.3 for $\Lambda = 5$.

In the following discussion, we will choose $\Lambda = 2$ to see how the self-trapped solutions behave in different scenarios. For plots with $z_i \neq 0$, we set the angular velocity to be $\bar{\Omega} = 0.5$ (thus $\epsilon = 0$ per definition 4.17), such that neither of the modes is energetically preferred. Therefore, the already busy plots don't get any more confusing than necessary. However, for any plots with $z_i \cong 0$, we will assume a faster rotation[6] of $\bar{\Omega} = 0.7$, such that the average over all trajectories is not simply a straight line but more insight about the system.

[4]The appearance and disappearance of the second set of cusps stem from the additional factor of $\sqrt{1-z^2}$ in the Josephson equation 4.23 compared to a simple sine function, which is discussed in [24]

[5]If we consider the other critical value $\Lambda_c = 1$, the backward-facing cusps appear for the π-oscillations as shown in figure A.4.

[6]Remember to keep $\bar{\Omega}$ within the regime given in 3.50, for which the two-mode approximation is valid.

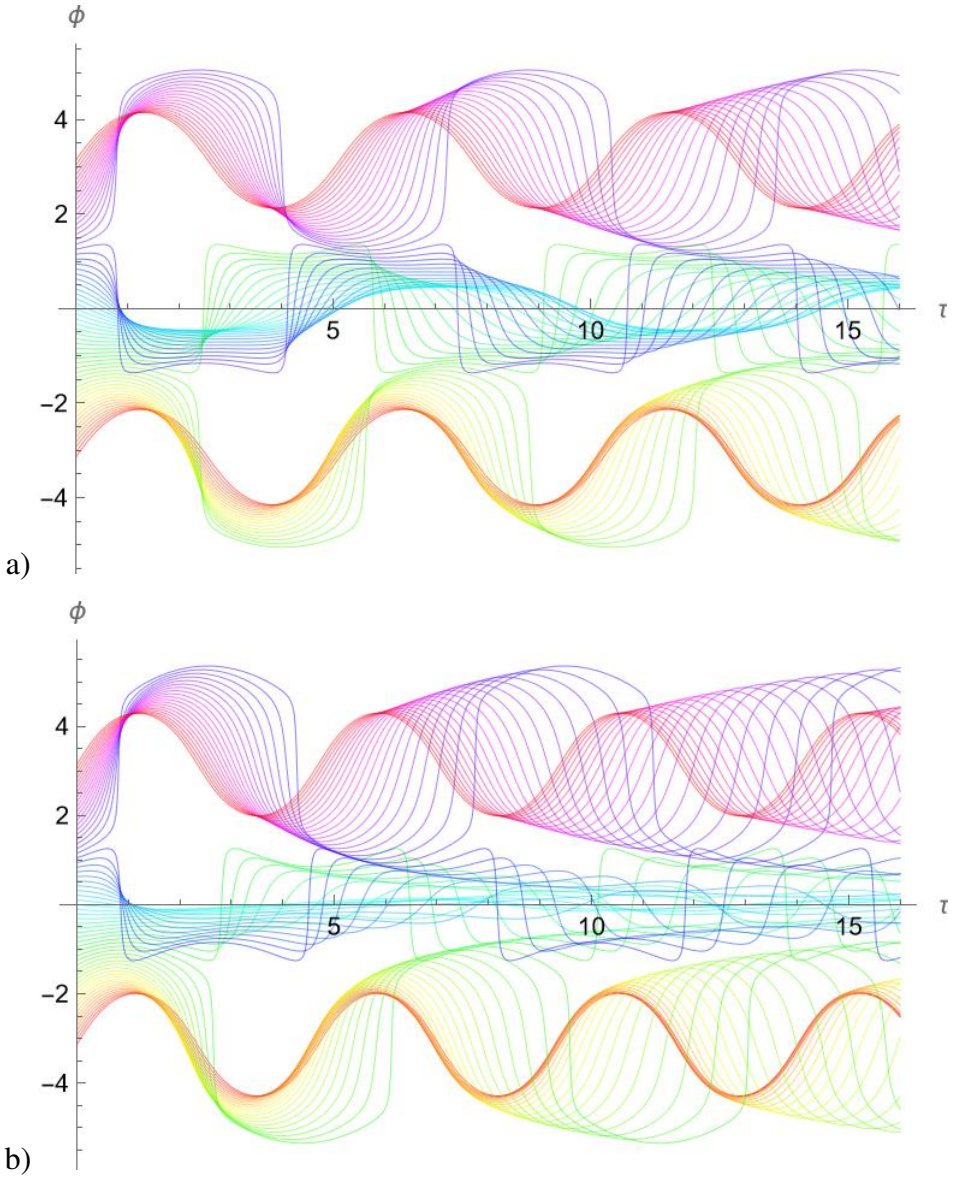

Figure 5.3.: Mean-field trajectories of the phase difference with $\bar{\Omega} = 0.5$ (thus $\epsilon = 0$) and $z_i = -0.7$ (only one side of Fock space, thus, breaking the symmetry), for the many different initial phase differences ϕ_i, denoted by the colors. Here, we tune the parameter Λ from a) $\Lambda = -0.75$ past the critical values $\Lambda_c = -1$, for which the stationary point $\phi = 0$ becomes unstable, to b) $\Lambda = -1.25$. Some trajectories with $\phi \approx 0$ (light blue) are self-trapped on one side of Fock space due to the bifurcation effect shown in figure 5.1

In the following chapters, we will discuss the match between classical trajectories in Fock space and actual quantum solutions. Here, we focus on cases similar to the classical trajectories shown below.

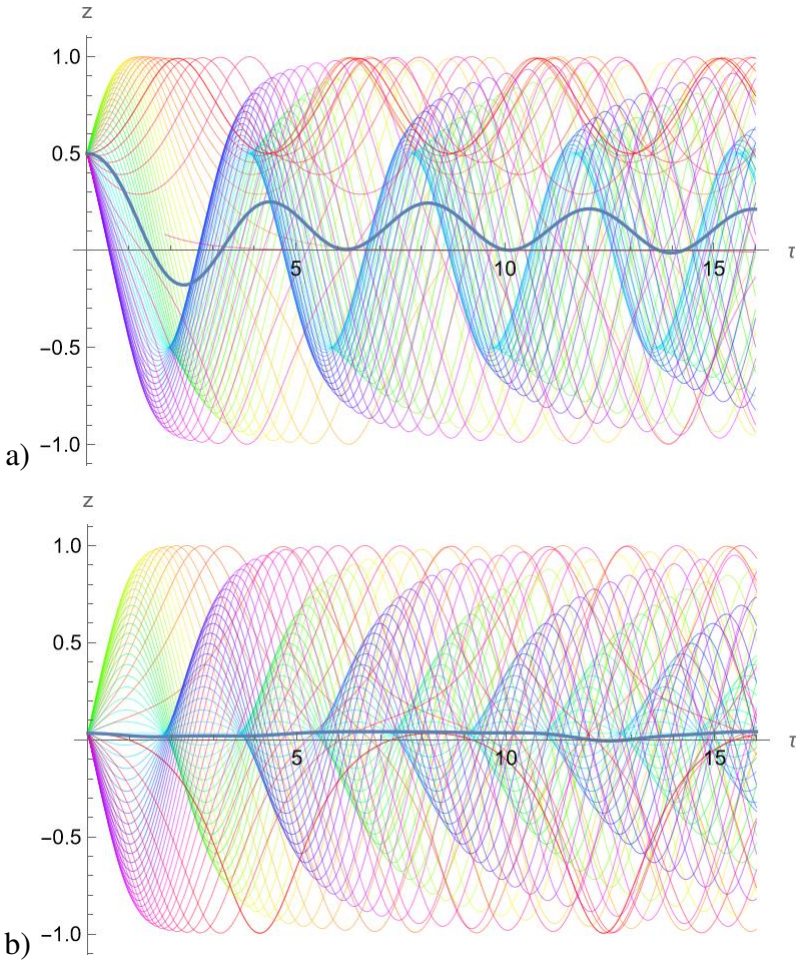

Figure 5.4.: Mean-field trajectories in Fock space over time derived from classical equations of motion (4.23, 4.24) with $\Lambda = 2$, for many different initial phase differences ϕ_i denoted by different colors and fixed initial population difference between the non-rotating $|0\rangle$ and rotating modes $|1\rangle$ given by $z_i = \frac{N_0 - N_1}{N}$ as a) $z_i = 0.5$ with $\bar{\Omega} = 0.5$ (thus $\epsilon = 0$) and b) $z_i \approx 0$ and $\bar{\Omega} = 0.7$ (thus $\epsilon \neq 0$). The blue lines denote the average over all trajectories.

5.2. Quantum Wavefunctions and SPDM

There are many different ways to investigate the full quantum version of the dynamics. The following results are produced by solving the time-dependent Schödinger equation. All findings have been confirmed by finding the eigenvalues of the tri-diagonal Hamiltonian in Fock basis 3.24 and comparing the results, which are identical. Furthermore, we calculated the expectation value of the population difference which turned out not to be an exact overlap with the classical expectation value as presented in several plots in the following sections. To explore the dynamics of the wavefunction over time, we have to pick an initial condition for the population difference and phase difference. In the following sections, we will consider different initial quantum states.

The visual representation of the complete eigensystem of the SPDM with its complex eigenvectors and real eigenvalues is rather intricate. We decided to show multiple plots in the appendix and focus on the Fock space predictions in this section, which turn out to be in perfect agreement with the expectation values of the quantum wavefunctions. To turn the eigensystem of the SPDM into a Fock space prediction, we start with the simple expression for the eigenstates with $a_\pm$ and $b_\pm$ being complex numbers

$$\Psi_\pm = a_\pm|0\rangle + b_\pm|1\rangle. \tag{5.1}$$

To find the population of the original two modes, we combine the eigenvalues with the respective weight of the eigenvectors. For that, we multiply the probability of each mode in the eigenvectors with their respective eigenvalues to get the occupation of the original two modes

$$N_\pm|\Psi_\pm|^2 = \underbrace{N_\pm|a_\pm|^2}_{N_{0,\pm}} + \underbrace{N_\pm|b_\pm|^2}_{N_{1,\pm}}. \tag{5.2}$$

From here, we can rearrange to get

$$N_0 = N_{0,+} + N_{0,-} = N_+|a_+|^2 + N_-|a_-|^2 \tag{5.3}$$

$$N_1 = N_{1,+} + N_{1,-} = N_+|b_+|^2 + N_-|b_-|^2. \tag{5.4}$$

Now that we know the population of each mode, we can also calculate $z = \frac{N_0 - N_1}{N}$ again, to get the relative population difference. This allows us, to represent the population of the non-rotating and rotating modes in Fock space.

$$z = \frac{1}{N}\Big[N_+\Big(|a_+|^2 - |b_+|^2\Big) + N_-\big(|a_-|^2 - |b_-|^2\big)\Big]. \tag{5.5}$$

Here, we can find the total number of particles $N = N_0 + N_1$ from equation 5.3 and 5.4. However, N is also one of the parameters we set in the Mathematica code. In the following chapters, we will compare the predictions of the population difference z with the expectation values of the wavefunctions and the average over the classical trajectories from the classical equations for motion.

In the appendix A.3.1, we plot the eigenvalues over time. Similarly for the eigenstates, we show the evolution of probabilities per component over time as well as their spinor representation on a sphere.

Fock State

To start with, we are looking at different Fock states, which are eigenstates of the interaction term of the Hamiltonian. As mentioned in the classical discussion, a Fock state has a defined particle difference and leaves the phase difference unrestricted, like a delta function in Fock space [16]. Since this is the quantum state we simulated with the classical trajectories, we see the best overlap between the two cases, as shown below and in the appendix in figure A.10. Also, the initial, relative population difference z_i from the classical case is exactly where the initial Fock state peaks. However, as shown in figure 5.6, the classical average and the quantum expectation value for z over time are slightly shifted. Consulting the SPDM, we can calculate the location of the BEC in Fock space over time, which gives exactly the same prediction as the quantum expectation value in figure, 5.6. For the SPDM we use the population of the non-rotating mode N_0 and the rotating mode N_1 to calculate the relative population difference $z = \frac{N_0 - N_1}{N}$ between them as shown in equation 5.5. The eigenvalues and eigenstates of the SPDM are presented in A.9. While the expectation value of the quantum case and the SPDM predictions are identical, the average over all classical trajectories from figure 5.4 agrees well at first but starts to slightly dissent from the other solutions after some time.

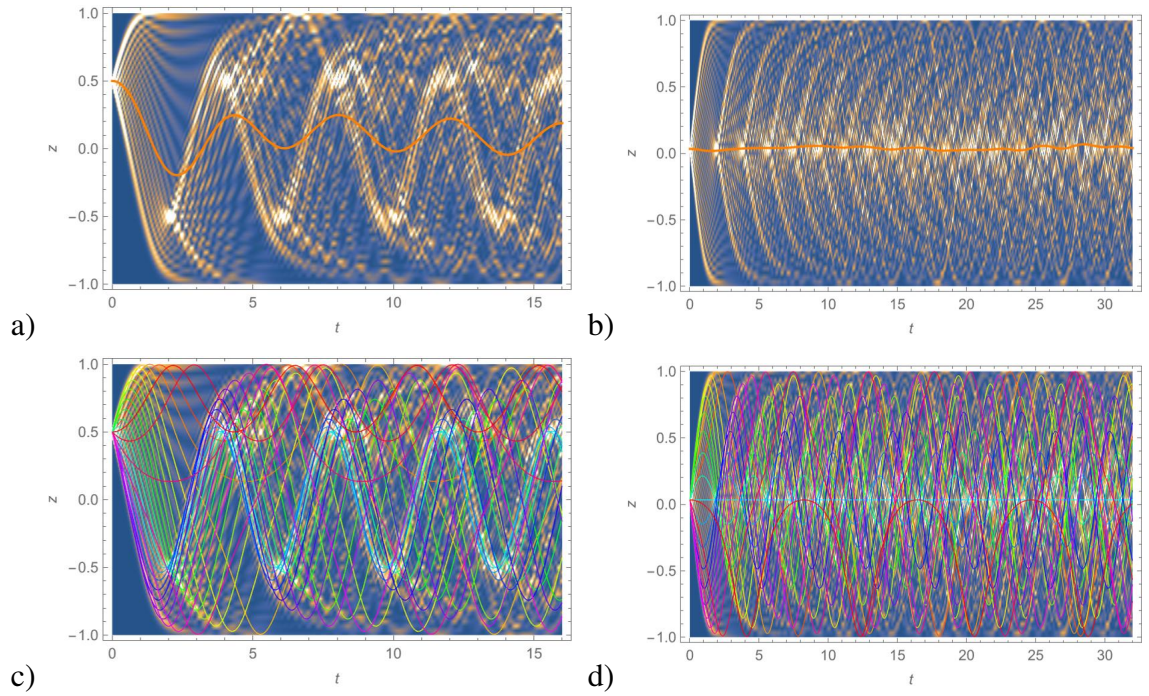

Figure 5.5.: Quantum trajectories in Fock space over time with $N = 60$, $\Lambda = 2$, and a) $z_i = 0.5$ and $\bar{\Omega} = 0.5$, or b) $z_i \approx 0$ and $\bar{\Omega} = 0.7$, compared to the classical trajectories from the previous chapter (plots c) and d) in the lower row). Here, we reduced the number of trajectories to ensure better visibility.

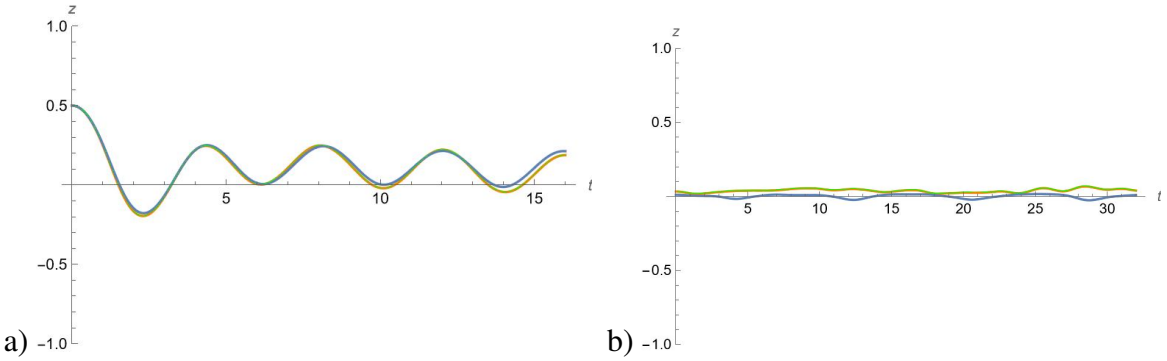

Figure 5.6.: Comparison of the classical average of trajectories (blue) with the expectation value (orange) of the quantum wavefunction and the SPDM prediction (green dots) according to equation 5.5 with $N = 60$, $\Lambda = 2$, a) $z_i = 0.5$ and $\bar{\Omega} = 0.5$, and b)$z_i \approx 0$ and $\bar{\Omega} = 0.7$. While the two quantum treatments lead to the same expectation, the classical average is slightly off.

To experimentally realize a Fock state, we must be able to control the population difference precisely. This is easier in the previously discussed double-well system due to the spatial separation. In the rotating trap, it is rather intricate to target particles individually with the rotation to excite them into the rotational state. The two seemingly simple scenarios are the edge states, where only one of the states is fully occupied. Here, all bosons are located either in the non-rotating state $z_i = 1$ with angular velocity $\bar{\Omega} = 0$ or in the rotational state $z_i = -1$ with $\bar{\Omega} = 1$, for which angular velocities the energy levels of the respective modes are lower than any other levels, remembering figure 3.3.2. However, both these choices of $\bar{\Omega}$ are outside the two-mode approximation. Additionally, since the trajectories start at the edge, the refocusing points will also be located there, making it hard to identify caustics.

Coherent State

A coherent state can be described as a Gaussian around a Fock state in Fock space [16]. Instead of just one defined initial population difference, it also includes neighboring Fock states with smaller probabilities. Thus, neither z_0 nor ϕ_0 are perfectly defined. The coherent state in Fock basis is given by [3]

$$cps[m, \theta, \phi] \equiv \sum_{m=-\frac{N}{2}}^{\frac{N}{2}} \sqrt{\binom{N}{\frac{N}{2}+m}} \left[\cos\left(\frac{\theta}{2}\right)\right]^N \left[e^{-i\phi}\tan\left(\frac{\theta}{2}\right)\right]^{\frac{N}{2}+m}, \tag{5.6}$$

where the sum over m includes all of Fock space, and $0 < \theta < \pi$ determines the location of the center of the distribution from the binomial coefficient in Fock space[7]. Fock states at the edge of Fock space, with $\theta \approx 0$ or π, are considered coherent states, which is further discussed in appendix A.3.3. Coherent states are the eigenstates of the lowering and raising operators and are sometimes referred to as the quantum states of the harmonic oscillator. To compare the quantum trajectories starting from a coherent state to the previously mentioned classical trajectories from figure 5.4, we use $\theta = \frac{2\pi}{3}$ for $z_i = 0.5$ and $\theta \approx \frac{\pi}{2}$ for $z_i \approx 0$, which leads to the coherent states shown in figure 5.7. Now, comparing the dynamics starting from a coherent state to the pseudo-Fock state is not exactly feasible, since now the population difference is less precisely defined and the phase difference more restricted. For a more accurate comparison, we would have to use a different truncated Wigner approximation. However, within the purpose of this thesis, we only remove some ϕ_i and leave z_i well-defined as the mean of the coherent state distribution. This leads to some higher inaccuracy when comparing the expectation values.

[7]Note, ϕ is an arbitrary phase that does not influence the appearance of the coherent state in the Fock basis.

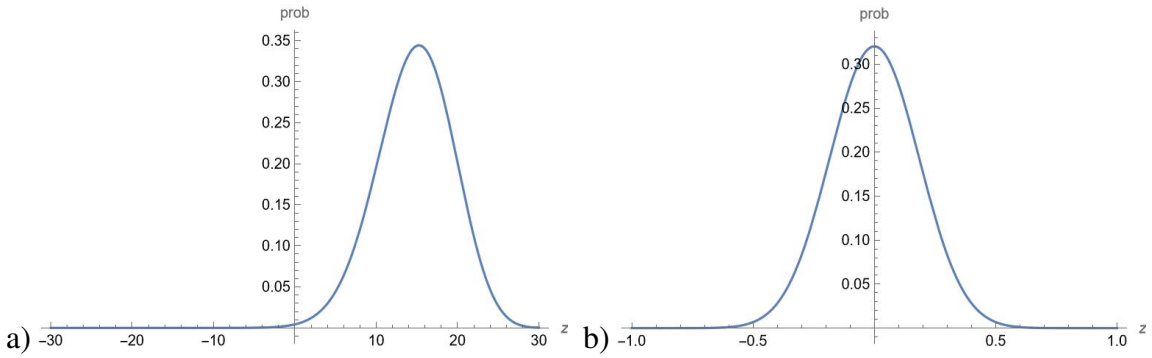

Figure 5.7.: Coherent states in Fock space with a) $\theta = \frac{2\pi}{3}$ for $z_i = 0.5$, and b) $\theta \approx \frac{\pi}{2}$ for $z_i \approx 0$. Here, $N = 60$, however, for larger N, the coherent state becomes more narrow.

Looking at the dynamics of the wavefunction in the symmetry broken case, figure 5.8 a), the whole system appears to be self-trapped around $\langle z \rangle \neq 0$. Therefore, only the trajectories for π-oscialltions (red lines) from 5.4 seem to contribute to the dynamics. For $z_i \approx 0$, the symmetry is not broken and all trajectories oscillate around $\langle z \rangle = 0$. Comparing the quantum expectation value with the average over all classical trajectories (blue line in figure 5.9) is only reasonable for the symmetric case, where the average over just the π-oscillations (red dashed line) is the same as the average over all trajectories. For the symmetry broken case, the average over only the π-oscillations (red dashed line) matches the trend of the quantum expectation value way better than the average over all trajectories (blue line), as shown in figure 5.9.

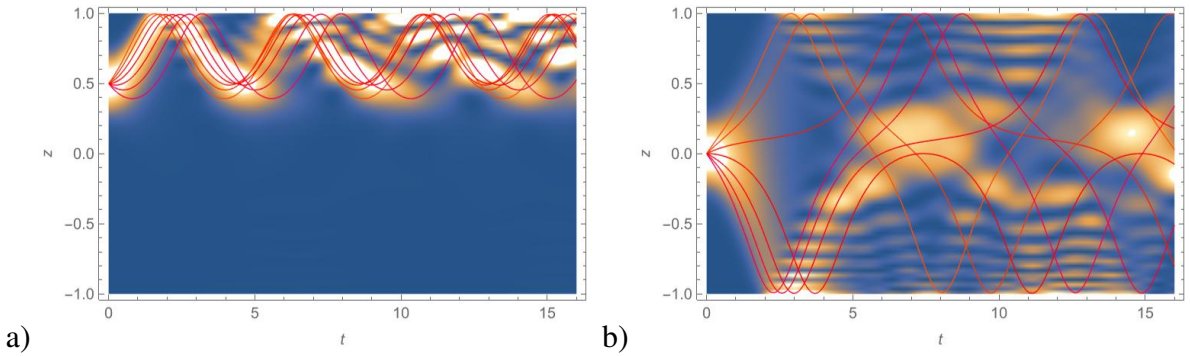

Figure 5.8.: Quantum trajectories in Fock space over time with $N = 60$, $\Lambda = 2$, compared to the classical trajectories from figure 5.4 with only π-oscillations a) with $z_i = 0.5$, $\theta = \frac{2\pi}{3}$ and $\bar{\Omega} = 0.5$, and b) with $z_i \approx 0$, $\theta \approx \frac{\pi}{2}$ and $\bar{\Omega} = 0.7$.

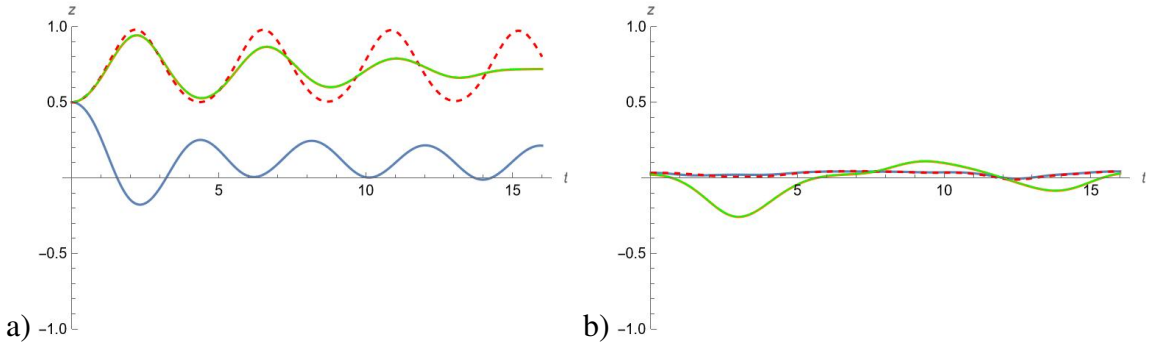

Figure 5.9.: Comparison of the classical average over all trajectories (blue) and over only the π-oscillations (dashed red) with the expectation value (orange) of the wavefunction and the SPDM prediction (green dots) according to equation 5.5 with $N = 60$, $\Lambda = 2$, a) $z_i = 0.5$, $\theta \approx \frac{2\pi}{3}$ and $\bar{\Omega} = 0.5$, and b)$z_i \approx 0$, $\theta \approx \frac{\pi}{2}$ and $\bar{\Omega} = 0.7$.

If we tune $\Lambda = -2$, the π-oscillations are no longer the ones that get self-trapped, as shown in figure 5.10. They oscillate around the stable $\langle z \rangle = 0$ fixed point at $\phi = 0$. Here, the plasma oscillations are now self-trapped but they do not contribute to the dynamics of a coherent state due to z_i being less well-defined, therefore, do not appear in figure 5.10.

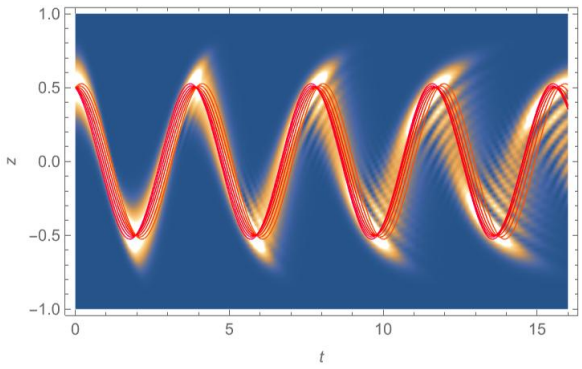

Figure 5.10.: Quantum trajectories in Fock space over time with $N = 60$, $\Lambda = -2$, $z_i = 0.5$, $\theta = \frac{2\pi}{3}$ and $\bar{\Omega} = 0.5$ compared to the classical trajectories from figure 5.4 with only π-oscillations.

Pegg Barnett State

A so-called Pegg Barnett (PB) state is an eigenstate of the hopping term of the Hamiltonian and the Fourier transform of a Fock state [25]

$$|\phi_p\rangle = \frac{1}{\sqrt{N+1}} \sum_{m=z_{min}}^{z_{max}} \exp(-im\phi_p)|m\rangle, \tag{5.7}$$

with $\phi_p = \frac{2\pi}{N+1}p$, where the initial phase ϕ_{pi} is well-defined, while all z_i in Fock space are possible. Thus, we will use a different truncated Wigner approximation, basically the Fourier transform of the previously discussed pseudo-Fock state. Both the quantum expectation value and the classical average are just constant in the center of Fock space, thus, not explicitly compared. Due to the symmetry, no self-trapping occurs. The dynamics for the PB state in 5.11 look similar to the Fock state dynamics in 5.5 b), however, slightly shifted and compressed. The appearing caustics are widespread across Fock space.

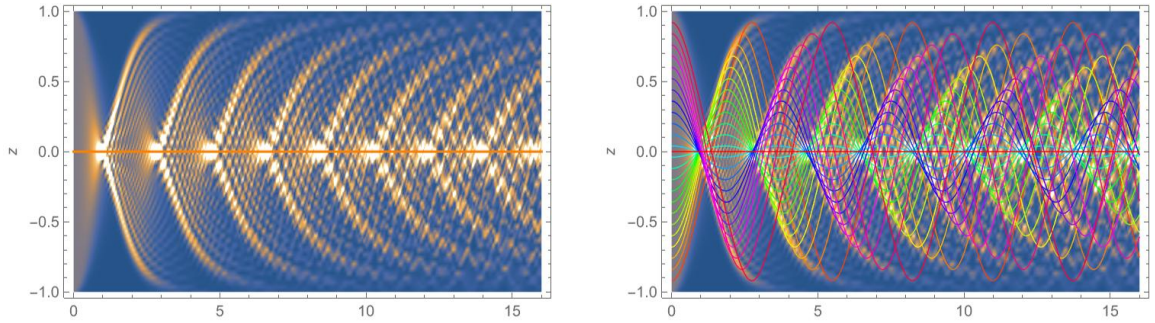

a) b)

Figure 5.11.: a) Quantum trajectories in Fock space over time with $N = 60$, $\Lambda = 2$, $\bar{\Omega} = 0.5$, b) compared to the classical trajectories with many different z_i and $\phi_i = 0$.

Eigenstate of Hamiltonian

Probably the easiest state to realize experimentally is the eigenstate of the Hamiltonian itself, which we calculated during the diagonalization. The lowest energy eigenstate, the groundstate, can be described as a Gaussian in Fock space. We can let the system settle into the groundstate[8] for the chosen parameter, before propagating after a sudden switch. The initial parameter Λ_i and $\bar{\Omega}_i$ determine different characteristics of the groundstate, as shown in 5.12.

[8]The groundstate is a symmetric linear combination of the non-rotating and rotating mode, while the first excited state is anti-symmetric.

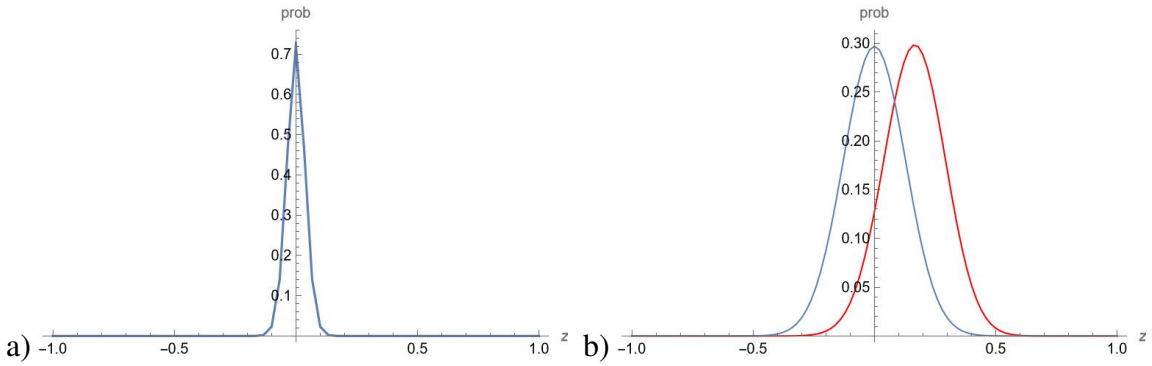

Figure 5.12.: Groundstates in Fock space for a) $\Lambda_i = 5000$ with $\bar{\Omega}_i = 0.5$, and b) $\Lambda_i = 0.5$ with $\bar{\Omega}_i = 0.5$ (blue) and $\bar{\Omega}_i = 1$ (red). Here, $N = 60$, however, precision could be enhanced with larger N, especially for the narrow state a).

Technically, $\bar{\Omega}_i$ shifts the Gaussian-like peak around in Fock space, where $\bar{\Omega}_i = 0$ is perfectly centered. Due to the restrictions of $\bar{\Omega}$ to lie within the two-mode approximation, only slight shifts are possible[9]. For large Λ, the groundstate becomes more narrow in Fock space e.g. more Fock state-like, while for small Λ it becomes very broad and more similar to a coherent state, as shown in 5.12. In the following, we present the wavefunctions for the unshifted groundstate with $\Lambda_i = 5000$ (which is very large to show clear trend) and $\Lambda_i = 0.5$, which we then let propagate with $\Lambda = 2$ and $\bar{\Omega} = 0.7$.

Once the groundstate has been realized, we can suddenly change the parameter, which is referred to as a sudden quench, and watch the dynamics of the system while it propagates. A sudden switch of the parameters is possible in the experiment due to the controllable setup. After the quench, the previous groundstate is no longer an eigenstate of the system and we can watch it evolve over time.

Due to the symmetry of the eigenstate in Fock space, no self-trapping occurs in either case. However, caustics are observable in the center of Fock space depending on the contributing trajectories, thus, initial phase differences. Since the eigenstates do not have a completely well-defined initial population difference z_i, not all initial phase differences might be possible. Even though the narrow groundstate is not quite a delta function in Fock space yet, it seems to reasonably match with all previously introduced phase differences, see figure 5.13 a). On the other hand, the broad groundstate has a very widespread initial population difference. Therefore, the choice of initial phase difference is more restricted and we lose some trajectories compared to the Fock state, which had valuable contributions to the caustics. As shown in figure 5.13 b), only the plasma oscillations seem to contribute. Thus, removing all other trajectories from the

[9] See figure A.12 for shifted narrow groundstate with $\bar{\Omega}_i = 20$, which is far outside the two-mode approximation.

classical case[10] gives a better overlap with the broad groundstate wavefunction. To get an even better idea of the actual classical trajectories corresponding to the groundstate propagation, one could apply a different truncated Wigner approximation for the initial condition in the classical case. Instead of a pseudo-Fock state, one would use the probability distribution from the initial quantum groundstate as the initial conditions for the classical trajectories.

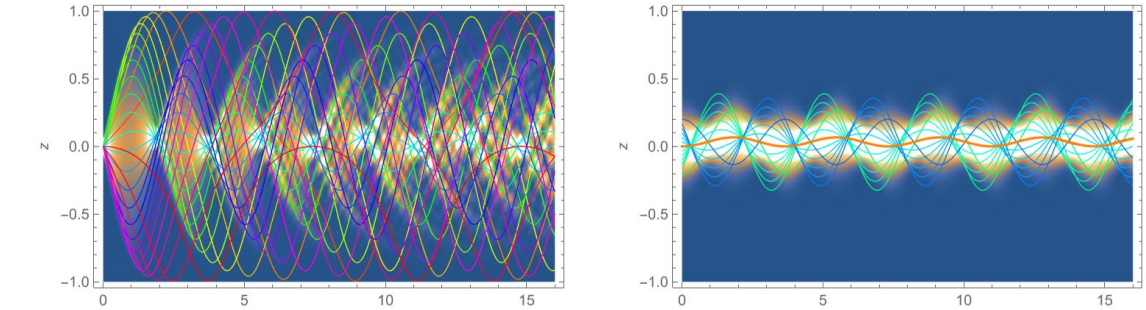

Figure 5.13.: Quantum trajectories in Fock space over time with $N = 60$, $\Lambda = 2$, $\bar{\Omega} = 0.7$, for initial groundstate with a) $\Lambda_i = 5000$ and b) $\Lambda_i = 0.5$. The narrow groundstate reasonably overlaps with the classical trajectories in with many different ϕ_i, while the broader groundstate seems to only match with the plasma oscillations.

Next, we compare the quantum expectation values with the classical average[11], in figure 5.14. For neither of the two initial groundstates, they match perfectly. However, for the narrow groundstate, the tendency agrees better. Since the classical trajectories were made from a pseudo-Fock state, the narrow groundstate might be approximated by a Fock state.

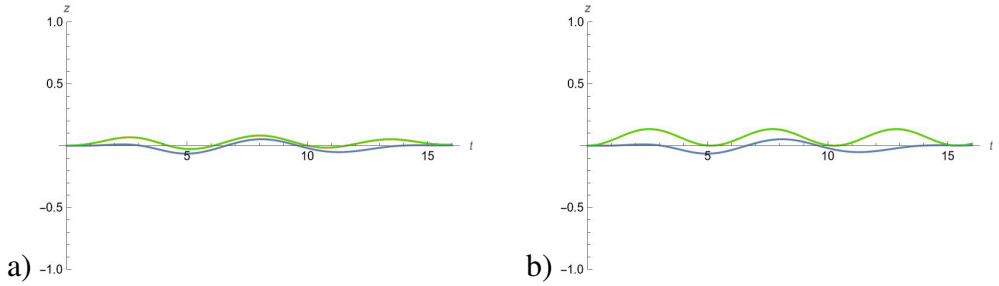

Figure 5.14.: Comparison of the average over the classical trajectories (blue) with the expectation value (orange) of the quantum wavefunction and the SPDM prediction (green dots), with $N = 60$, $\Lambda = 0.5$, $z_i = 0$, $\bar{\Omega} = 0.7$, for initial groundstate with a) $\Lambda_i = 5000$ (narrow groundstate) and b) $\Lambda = 0.5$ (broad groundstate).

[10] Similar to the adjustments we had to make for the classical trajectories to match the coherent state.

[11] Both quantum predictions are the same, and due to the symmetry, the average over just the plasma oscillations as the average over all trajectories.

6. Conclusion

Using an atomic BEC model, we investigated the dynamical properties of many-body quantum systems around instabilities and the concomitant bifurcation leading to phase transitions.

Within the many-body theory and two-mode approximation, we were able to map the BEC in a toroidal trap onto a double-well system. We found a spontaneous phase transition to occur at a critical value of $|\Lambda_c| = 1$, which breaks $\mathbf{Z}_2$ symmetry. Below the critical value, the system is in the symmetric phase, where bosons strive to equally populate both the non-rotating and the rotating modes, considering the angular velocity of the trap $\bar{\Omega} = 0.5$ does not bias the system. For a slower rotation, bosons prefer the non-rotating mode, while faster rotations excite more bosons into the rotating mode. If $|\Lambda_c|$ exceeds the critical value, the system enters the symmetry broken phase, where one mode is dominantly populated, depending on the initial conditions of the system. If we start off with more bosons in either the non-rotating or rotating mode, the same state is preferred in the symmetry broken phase. This is referred to as self-trapping. In both phases, we identify cusp catastrophes appearing when the trajectories in the collective dynamics attempt to refocus. This can be further analyzed using catastrophe theory. In the symmetric phase, both the plasma and the π-oscillations independently create cusps, however, facing opposite directions. The directions of the cusps for each of the oscillations entirely depends on the sign of Λ, as shown in figure A.3 b) for $\Lambda = -0.5$ and d) for $\Lambda = 0.5$. For negative Λ, plasma oscillations form backward-facing cusps (blue trajectories), while the cusps formed by π-oscillations face the opposite direction (red trajectories). For positive Λ, the directions are switched. Entering the symmetry broken phase, the backward-facing cusps vanish. Here, some trajectories only oscillate on one side of Fock space due to self-trapping, causing them to miss the refocusing entirely. This can be considered a dynamical phase transition. Whether plasma oscillations or π-oscillations become self-trapped, thus, cease to form (backward-facing) cusps, again depends on the sign of Λ. In chapter 5, we explicitly discussed the phase transition at $\Lambda = -1$, where plasma oscillations (blue trajectories) become self-trapped and no longer form backward-facing cusps, as shown in figure 5.2. The phase transition at $\Lambda = 1$ is shown in figure A.4 with self-trapped π-oscillations (red trajectories).

One of the main theoretical tools we used in this thesis is the so-called truncated Wigner approximation [13], [20],[30],[34] where one uses many classical trajectories (each being a solution of the mean-field equations of motion with initial conditions sampled from a quantum probability distribution) to mimic the dynamics of the quantum (many-body) wavefunction. The case of an initial Fock state is particularly simple because the number difference is completely defined and so the phase difference is completely undefined (all phases are equally probable). The trajectories generically undergo focusing to form caustics, especially fold and cusp caustics which according to catastrophe theory are the only stable singularities in two dimensions (e.g. when plotting number difference versus time). Depending on the choice of an initial quantum state, the quantum wavefunctions match fairly well with the mean-field trajectories. A coherent state living at the edge of Fock space is also a Fock state. Here, the refocusing of the trajectories happens too close to the edge to witness clear cusp formation. To find a centered Fock state, that is experimentally easy to create, we investigate the eigenstates of the system. Letting it settle into the groundstate for very large Λ, leads to a rather narrow probability distribution around the center of Fock space, where the population difference is rather well defined and we can approximate the ground state as a Fock state, without having to sacrifice any trajectories from the unrestricted phase differences.

6.1. Outlook

Following the results of this thesis, one can look further into the caustics we saw appearing in the collective dynamics using catastrophe theory. Here, we can investigate the appearance and behavior of vortices. On the other hand, one could follow up on the dynamical and energetic instabilities found in the toroidal trap system. Here, one could investigate the decay rates of the different instabilities. One can also make connections to hawking radiation in sonic black holes from the depletion. To further deepen our understanding of BEC in a toroidal trap, one could include a third mode and investigate its comparability to a triple well system.

Bibliography

[1] N. W. Ashcroft and N. D. Mermin. *Solid State Physics*. Holt-Saunders, 1976.

[2] S. Baharian and G. Baym. Bose-Einstein condensates in toroidal traps: Instabilities, swallow-tail loops, and self-trapping. *Phys. Rev. A*, 87:013619, Jan 2013.

[3] S. Barnett and P. Radmore. *Methods in Theoretical Quantum Optics*. Oxford University Press, 2002.

[4] Y. Cai, D. G. Allman, P. Sabharwal, and K. C. Wright. Persistent currents in rings of ultracold fermionic atoms. *Phys. Rev. Lett.*, 128:150401, Apr 2022.

[5] G. K. Campbell. website: Atom circuits.

[6] S. Eckel, J. G. Lee, F. Jendrzejewski, N. Murray, C. W. Clark, C. J. Lobb, W. D. Phillips, M. Edwards, and G. K. Campbell. Hysteresis in a quantized superfluid 'atomtronic' circuit. *Nature*, 506:200–203, 2014.

[7] A. L. Fetter. Nonuniform states of an imperfect Bose gas. *Ann. Phys.*, 70(1):67–101, 1972.

[8] A. L. Fetter. Rotating trapped Bose-Einstein condensates. *Rev. Mod. Phys.*, 81:647–691, May 2009.

[9] C. W. Gardiner. Particle-number-conserving Bogoliubov method which demonstrates the validity of the time-dependent Gross-Pitaevskii equation for a highly condensed Bose gas. *Phys. Rev. A*, 56:1414–1423, Aug 1997.

[10] R. Gati and M. K. Oberthaler. A bosonic Josephson junction. *Journal of Physics B: Atomic, Molecular and Optical Physics*, 40(10):R61–R89, may 2007.

[11] Griffin. *Bose-Einstein Condensation*. Cambridge University Press, 1995.

[12] A. P. Hines, R. H. McKenzie, and G. J. Milburn. Entanglement of two-mode Bose-Einstein condensates. *Phys. Rev. A*, 67:013609, Jan 2003.

[13] J. Javanainen and J. Ruostekoski. Emergent classicality in continuous quantum measurements. *New J. Phys.*, 15, 01 2013.

[14] G. Krahn and D. O'Dell. Classical versus quantum dynamics of the atomic Josephson junction. *J. Phys. B - AT MOL OPT*, 42, 08 2009.

[15] L. Landau and E. Lifshitz. *Mechanics*. Pergamon, 1960.

[16] U. Leonhardt. *Essential Quantum Optics: From Quantum Measurements to Black Holes*. Cambridge University Press, 2010.

[17] U. Leonhardt, T. Kiss, and P. Öhberg. Theory of elementary excitations in unstable Bose-Einstein condensates and the instability of sonic horizons. *Phys. Rev. A*, 67:033602, Mar 2003.

[18] I. Lesanovsky and W. von Klitzing. Time-averaged adiabatic potentials: Versatile matter-wave guides and atom traps. *Phys. Rev. Lett.*, 99:083001, Aug 2007.

[19] M. Machholm, C. J. Pethick, and H. Smith. Band structure, elementary excitations, and stability of a Bose-Einstein condensate in a periodic potential. *Phys. Rev. A*, 67(5), 5 2003.

[20] A. D. Martin and J. Ruostekoski. Quantum and thermal effects of dark solitons in a one-dimensional Bose gas. *Phys. Rev. Lett.*, 104:194102, May 2010.

[21] C. Menotti, A. Smerzi, and A. Trombettoni. Superfluid dynamics of a Bose–Einstein condensate in a periodic potential. *New J. Phys.*, 5:112–112, sep 2003.

[22] G. J. Milburn, J. Corney, E. M. Wright, and D. F. Walls. Quantum dynamics of an atomic Bose-Einstein condensate in a double-well potential. *Phys. Rev. A*, 55:4318–4324, Jun 1997.

[23] J. Mumford. *Singularities in a BEC in a double well potential*. PhD thesis, McMaster University, 2017.

[24] J. Mumford, W. Kirkby, and D. H. J. O'Dell. Catastrophes in non-equilibrium many-particle wave functions: universality and critical scaling. *J. Phys. B - AT MOL OPT*, 50(4):044005, feb 2017.

[25] J. Mumford, E. Turner, D. W. L. Sprung, and D. H. J. O'Dell. Quantum spin dynamics in Fock space following quenches: Caustics and vortices. *Phys. Rev. Lett.*, 122:170402, May 2019.

[26] N. Murray, M. Krygier, M. Edwards, K. C. Wright, G. K. Campbell, and C. W. Clark. Probing the circulation of ring-shaped Bose-Einstein condensates. *Phys. Rev. A*, 88:053615, Nov 2013.

[27] D. O'Dell. website: Duncan o'dell.

[28] C. J. Pethick and H. Smith. *Bose–Einstein Condensation in Dilute Gases*. Cambridge University Press, 2 edition, 2008.

[29] L. Pitaevskii and S. Stringari. *Bose-Einstein Condensation and Superfluidity*. Oxford University Press, 2016.

[30] A. Polkovnikov. Phase space representation of quantum dynamics. *Ann. Phys.*, 325(8):1790–1852, 2010.

[31] S. Raghavan, A. Smerzi, S. Fantoni, and S. R. Shenoy. Coherent oscillations between two weakly coupled Bose-Einstein condensates: Josephson effects, π oscillations, and macroscopic quantum self-trapping. *Phys. Rev. A*, 59:620–633, Jan 1999.

[32] A. Ramanathan, K. C. Wright, S. R. Muniz, M. Zelan, W. T. Hill, C. J. Lobb, K. Helmerson, W. D. Phillips, and G. K. Campbell. Superflow in a toroidal Bose-Einstein condensate: An atom circuit with a tunable weak link. *Phys. Rev. Lett.*, 106:130401, Mar 2011.

[33] D. S. Rokhsar. Dilute Bose gas in a torus: vortices and persistent currents. *arXiv: Condensed Matter*, 1997.

[34] J. Ruostekoski and L. Isella. Dissipative quantum dynamics of bosonic atoms in a shallow 1d optical lattice. *Phys. Rev. Lett.*, 95:110403, 10 2005.

[35] J. Schwinger. On angular momentum. 1952.

[36] S. Sinha and Y. Castin. Dynamic instability of a rotating Bose-Einstein condensate. *Phys. Rev. Lett.*, 87:190402, Oct 2001.

[37] A. Smerzi, S. Fantoni, S. Giovanazzi, and S. R. Shenoy. Quantum coherent atomic tunneling between two trapped Bose-Einstein condensates. *Phys. Rev. Lett.*, 79:4950–4953, Dec 1997.

[38] M. Ueda and A. J. Leggett. Ground-state properties of a rotating Bose-Einstein condensate with attractive interaction. *Phys. Rev. Lett.*, 83:1489–1493, Aug 1999.

[39] R. M. W. van Bijnen, D. H. J. O'Dell, N. G. Parker, and A. M. Martin. Dynamical instability of a rotating dipolar Bose-Einstein condensate. *Phys. Rev. Lett.*, 98:150401, Apr 2007.

[40] A. Vardi and J. R. Anglin. Bose-Einstein condensates beyond mean field theory: Quantum backreaction as decoherence. *Phys. Rev. Lett.*, 86:568–571, Jan 2001.

[41] G. Vasilakis, A. Roussou, J. Smyrnakis, M. Magiropoulos, W. von Klitzing, and G. M. Kavoulakis. Transition from the mean-field to the bosonic Laughlin state in a rotating Bose-Einstein condensate. *Phys. Rev. A*, 100:023606, Aug 2019.

[42] K. C. Wright, R. B. Blakestad, C. J. Lobb, W. D. Phillips, and G. K. Campbell. Threshold for creating excitations in a stirred superfluid ring. *Phys. Rev. A*, 88:063633, Dec 2013.

[43] B. Wu and Q. Niu. Superfluidity of Bose Einstein condensate in an optical lattice: Landau Zener tunnelling and dynamical instability. *New J. Phys.*, 5:104, 07 2003.

[44] T. Zibold, E. Nicklas, C. Gross, and M. K. Oberthaler. Classical bifurcation at the transition from Rabi to Josephson dynamics. *Phys. Rev. Lett.*, 105:204101, Nov 2010.

A. Appendix

A.1. Josephson Equations in the Toroidal Trap

In this chapter, we show more details on deriving the equations of motion for the two-mode BEC in a toroidal trap. Starting from the rotating frame GPE, which also includes the disorder potential

$$i\partial_t \Psi_c = \Big[-\frac{1}{2}\frac{\partial^2}{\partial\theta^2} + i\Omega\frac{\partial}{\partial\theta} + \eta|\Psi_c|^2 + 2\upsilon\cos(\theta)\Big]\Psi_c. \tag{A.1}$$

Using the two-mode condensate wavefunction $|\Psi_c\rangle = \sqrt{N}\Big[c_0(t)|0\rangle + c_1(t)|1\rangle\Big]$ and the position vector $|r\rangle = (R,\theta)$ we can find the normalized non-interacting single-particle eigenstates $\Psi_c = \langle \mathbf{r}|\Psi_c\rangle = \frac{1}{\sqrt{2\pi R}}e^{ij_c\theta}$ to be

$$\Psi_c = \sqrt{\frac{N}{2\pi R}}\Big[c_0(t) + e^{i\theta}c_1(t)\Big]. \tag{A.2}$$

Using equation A.2 in the GPE A.1, we find the following coupled equations [2]

$$i\dot{c}_0 = \upsilon c_1 + \Big[2 - |c_0|^2\Big]c_0 \tag{A.3}$$

$$i\dot{c}_1 = \upsilon c_0 + \Big[2 - |c_1|^2\Big]c_1 + \Big[\frac{1}{2} - \bar{\Omega}\Big]c_1. \tag{A.4}$$

Expressing the complex numbers as $c_j = |c_j|e^{i\phi_j}$ again allows us to switch to the parameter z and ϕ from the definition 4.18 later.

$$\begin{aligned} i|\dot{c}_0| - |c_0|\dot{\phi}_0 &= \upsilon|c_1|\big[\cos(\phi) - i\sin(\phi)\big] + \eta N\Big[2 - |c_0|^2\Big]|c_0| \\ i|\dot{c}_1| - |c_1|\dot{\phi}_1 &= \upsilon|c_0|\big[\cos(\phi) + i\sin(\phi)\big] + \eta N\Big[2 - |c_1|^2\Big]|c_1| + \Big[\frac{1}{2} - \bar{\Omega}\Big]|c_1|. \end{aligned} \tag{A.5}$$

Now, we can separate equation A.5 into real and imaginary parts. Let's focus on the imaginary equations first, which read as follows

$$i|\dot{c}_0| = -iv|c_1|\sin(\phi) \tag{A.6}$$
$$i|\dot{c}_1| = iv|c_0|\sin(\phi). \tag{A.7}$$

If we multiply them with either $|c_0|$ or $|c_1|$ respectively leads to

$$|c_0||\dot{c}_0| = \frac{1}{2}\frac{d}{dt}(|c_0|^2) = -v|c_0||c_1|\sin(\phi) \tag{A.8}$$
$$|c_1||\dot{c}_1| = \frac{1}{2}\frac{d}{dt}(|c_1|^2) = v|c_1||c_0|\sin(\phi). \tag{A.9}$$

Now, we can subtract the latter from the first and finally use the definition $z = |c_0|^2 - |c_1|^2$, such that

$$\frac{1}{2}\frac{dz}{dt} = -v\sqrt{1-z^2}\sin(\phi). \tag{A.10}$$

Lastly, we have to rescale the time $\tau = 2vt$ and arrive at

$$\frac{dz}{d\tau} = -\sqrt{1-z^2}\sin(\phi). \tag{A.11}$$

This is the same as the equation of motion 3.40 as the double-well case.

Now, we will calculate the second equation of motion with a similar procedure using the real equations from A.5, which look like

$$-|c_0|\dot{\phi}_0 = v|c_1|\cos(\phi) + \eta N\Big[2 - |c_0|^2\Big]|c_0| \tag{A.12}$$
$$-|c_1|\dot{\phi}_1 = v|c_0|\cos(\phi) + \eta N\Big[2 - |c_1|^2\Big]|c_1| + \Big[\frac{1}{2} - \bar{\Omega}\Big]|c_1|. \tag{A.13}$$

Multiplying them with $|c_0|$ and $|c_0|$ respectively and taking the difference lets us use z and ϕ from 4.18 again, which leads to

$$\frac{d\phi}{dt} = 2\upsilon\cos(\phi)\frac{z}{\sqrt{1-z^2}} + \eta N z + \left[\frac{1}{2} - \bar{\Omega}\right]. \tag{A.14}$$

Now rescaling the time $\tau = 2\upsilon t$ leads to

$$\frac{d\phi}{dt} = \cos(\phi)\frac{z}{\sqrt{1-z^2}} + \underbrace{\frac{\eta N}{2\upsilon}}_{\Lambda} z + \underbrace{\frac{\left[\frac{1}{2} - \bar{\Omega}\right]}{2\upsilon}}_{\epsilon}, \tag{A.15}$$

where we are using the definitions for ϵ and Λ from 4.17 again[1]. Therefore, the second equation of motion turns out the be

$$\frac{d\phi}{dt} = \cos(\phi)\frac{z}{\sqrt{1-z^2}} + \Lambda z + \epsilon, \tag{A.16}$$

which again agrees with the equation of motion 3.39 from the double-well case.

[1]Remember, ϕ in the toroidal trap has a global negative sign compared to the one in the double-well.

A.2. Classical Trajectories

Parameter

To deepen the understanding of the role each parameter (Λ, $\bar{\Omega}$ and z_i) plays for the classical trajectories, we present some examples of tuning one parameter while holding the other parameters constant with $N = 60$.

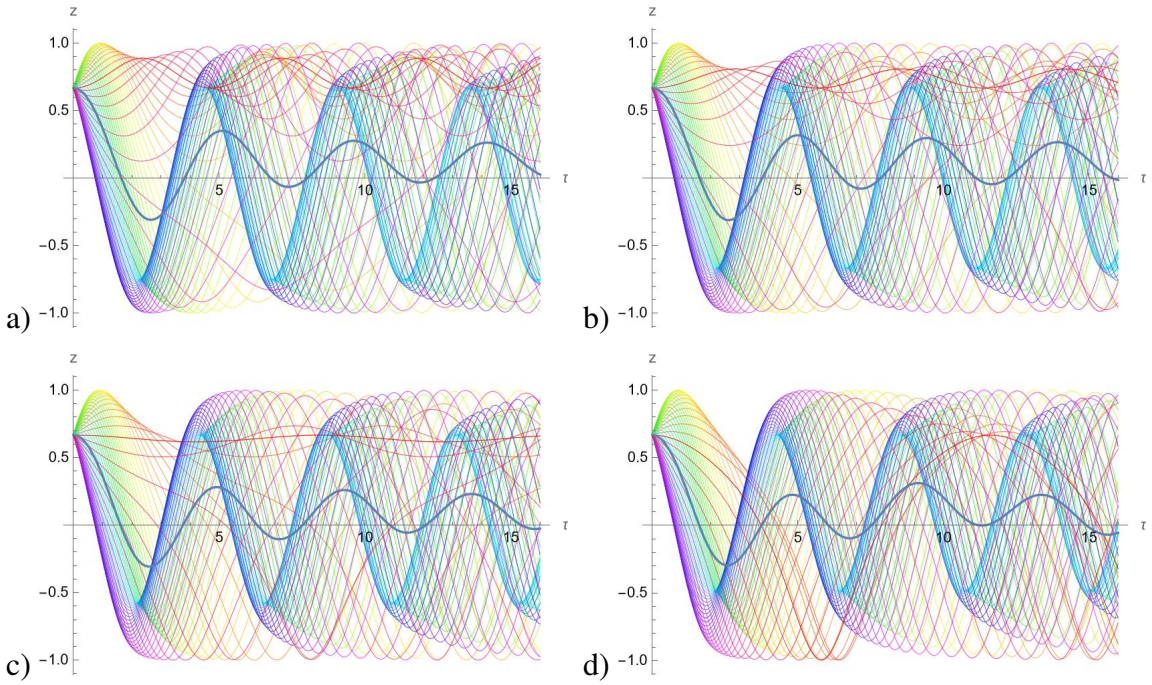

Figure A.1.: Mean-field trajectories in Fock space $z_i = 0.\bar{6}$ and $\Lambda = 1.5$, for many different initial phase differences ϕ_i. Here, we tune $\bar{\Omega}$ to increase from a) to c) within the valid two-mode approximation region a) $\bar{\Omega} = 0.25$, b) $\bar{\Omega} = 0$, c) $\bar{\Omega} = 0.75$ and outside the valid two-mode approximation d) $\bar{\Omega} = 1$.

Looking at the initial state with most bosons in the non-rotating state $z = 0.6$ in the regime $\Lambda = 1.5$, where self-trapping of the π-oscilaltions occurs in the non-rotating mode, increasing the angular velocity $\bar{\Omega}$ (figure A.1) leads to a decrease in the amount of self-trapped trajectories. Here, bosons get more easily excited into the rotating mode. We present $\bar{\Omega}$ outside the two-mode approximation to show the exaggerated effect.

For $\Lambda = 2$ and $\bar{\Omega} = 0.5$ (no preferred mode), we can see how z_i determines on which the side of Fock space the π-oscillations get trapped (figure A.2). For $z_i = 0$, no self-trapping occurs since no new stable fixed points appear and all π-oscillations disappear, as shown in figure A.6.

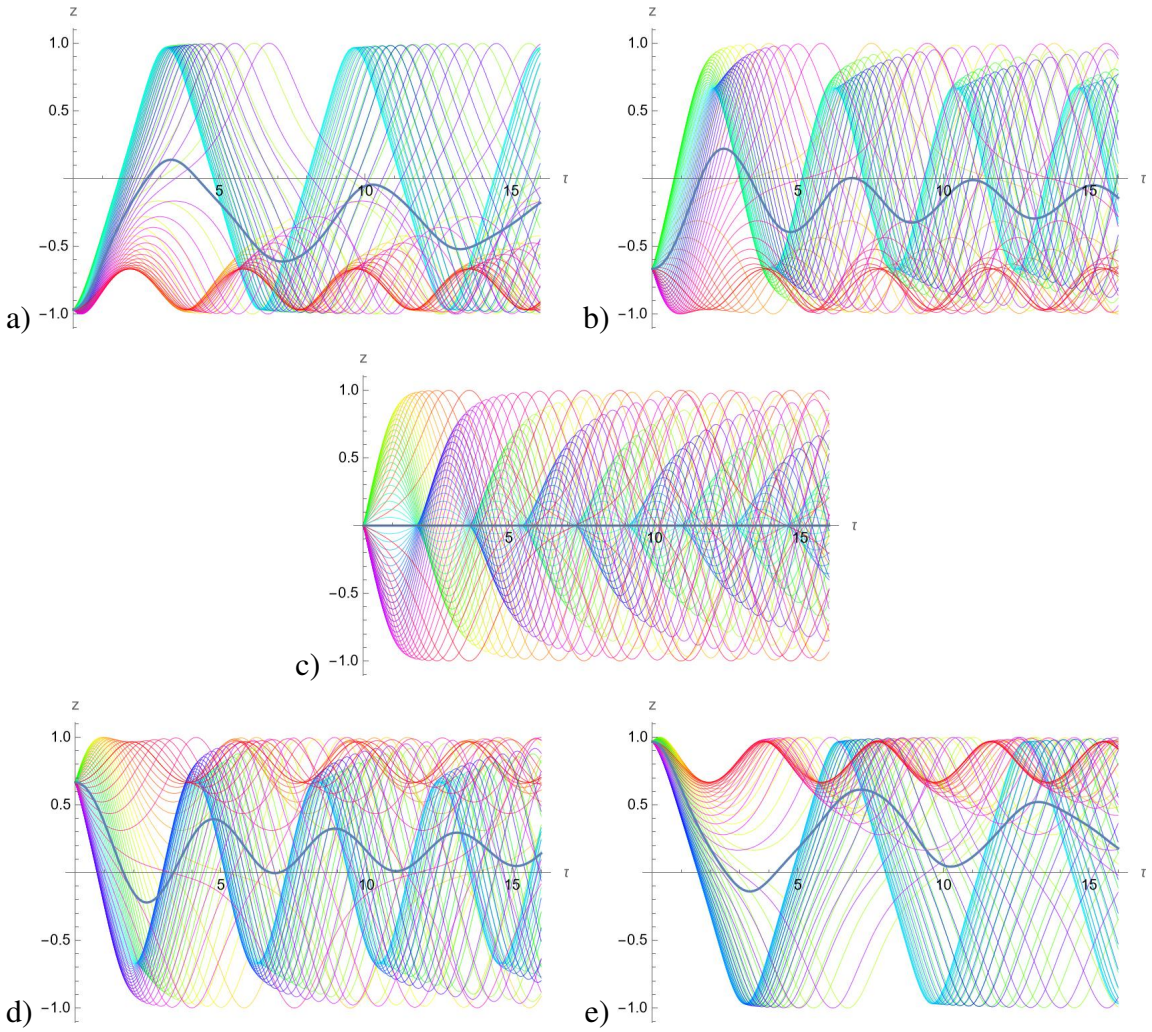

Figure A.2.: Mean-field trajectories in Fock space $\bar{\Omega} = 0.5$ and $\Lambda = 2$, for many different initial phase differences ϕ_i. Here, we tune z_i to increase from a) to e) with a) $z_i \approx -1$, b)$z_i = 0.\bar{6}$, c)$z_i = 0$ d) $z_i = 0.\bar{6}$, e) $z_i \approx 1$.

Keeping $z_i = 0.\bar{6}$ and $\bar{\Omega} = 0.5$ (no preferred mode), tunig Λ (figure A.3) determines whether self-trapping occurs or not. The sign of Λ decides if plasma oscillations (blue linse) or π-oscillations (red lines) become self-trapped. If $\Lambda \gg \Lambda_c$, more trajectories become self-trapped. For $\Lambda = 0$, the double cusps share the same focus point.

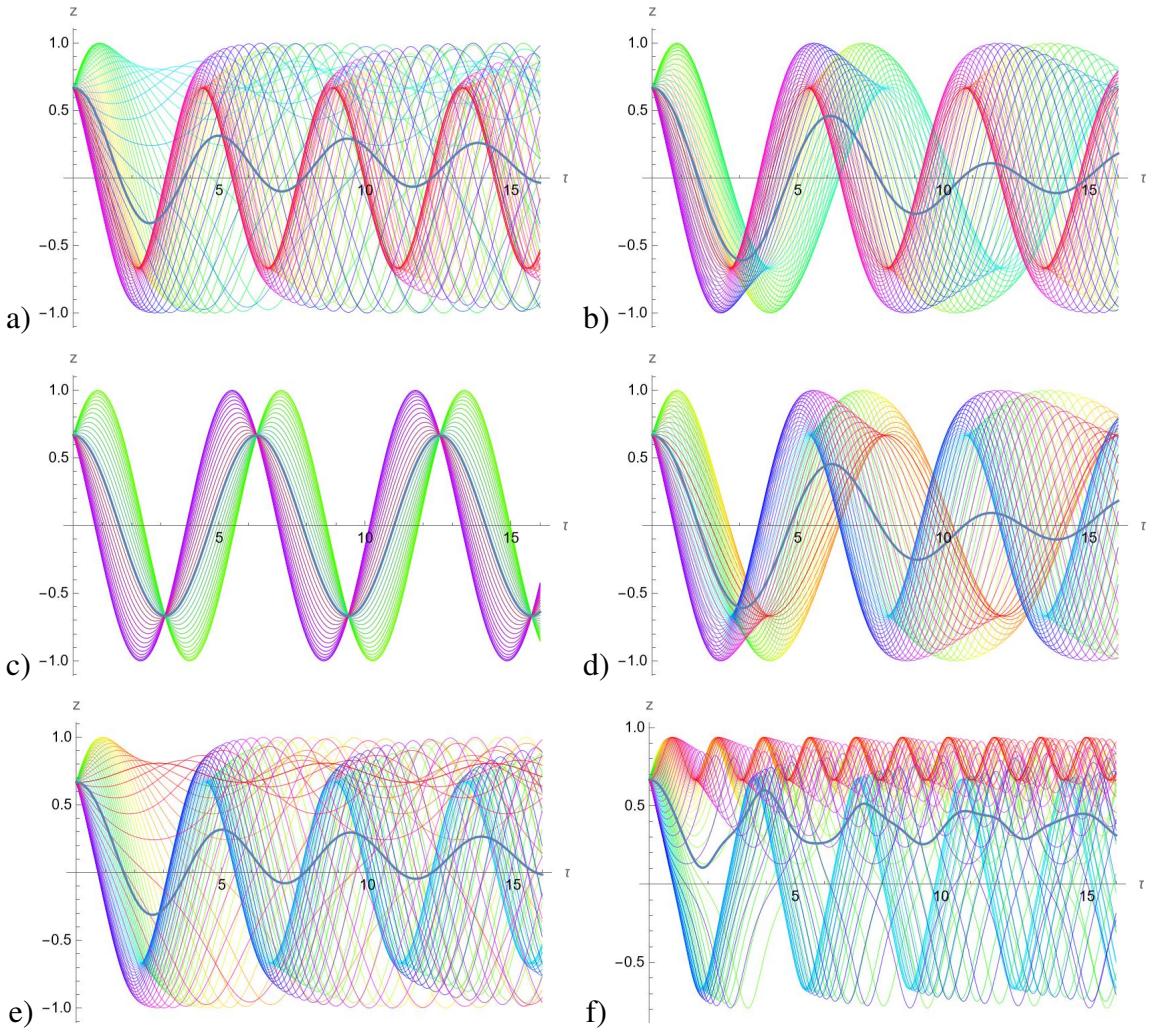

Figure A.3.: Mean-field trajectories in Fock space $\bar{\Omega} = 0.5$ and $z_i = 0.\bar{6}$, for many different initial phase differences ϕ_i. Here, we tune Λ to increase from a) to f) with a) $\Lambda = -1.5$, b)$\Lambda = -0.5$, c) $\Lambda \approx 0$, d) $\Lambda = 0.5$, e) $\Lambda = 1.5$, f) $\Lambda = 5$

Self-trapping in π-Oscillation

As discussed in chapter 5, the system undergoes a topological phase transition for $|\Lambda| = 1$. Initially, we showed the plasma oscillations getting trapped on one side of Fock space for $\Lambda < -1$, causing some of the cusps catastrophes in the collective dynamics to vanish. Here, we also present the $\Lambda > 1$ case, where the π-oscillations are self-trapped. The self-trapping is shown in figure A.4, where some of the red trajectories oscillate around a fixed value on one side of Fock space, which is equivalent to trajectories remaining on one hemisphere in figure A.7. In phase space, the red lines remain close to their initial value, indicating a very small oscillation. In these plots, we only show the trajectories for the initial population difference $z_i = -0.7$, causing symmetry breaking. (See full symmetric case with $z_i = \pm 0.7$ in figure A.5)).

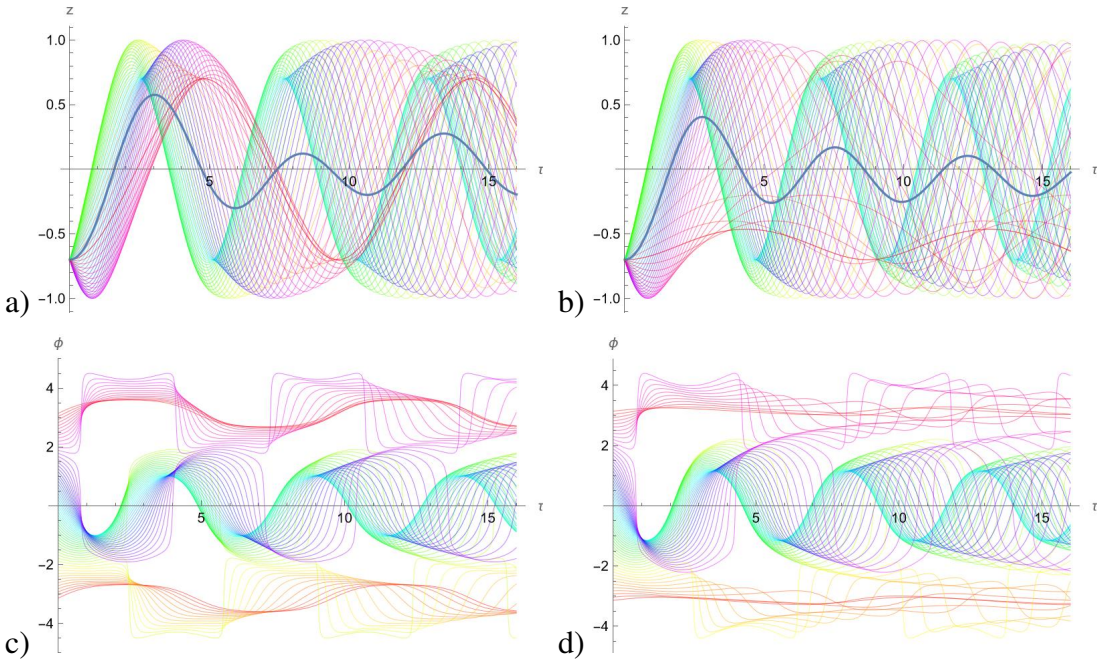

Figure A.4.: Mean-field trajectories of the population difference (upper row) and phase difference (lower row) with $\bar{\Omega} = 0.5$ and $z_i = -0.7$, for many different initial phase differences ϕ_i. Here, we tune the parameter Λ from $\Lambda = 0.75$ (left), to $\Lambda = 1.25$ (right) for which some π-oscillations (red lines) become self-trapped.

In figure A.7, we show the trajectories in a phase-space diagram. Here, we choose $\Lambda = 0$, where plasma and π-oscillations have the same elliptical shape. $\Lambda > 1$ causes the previously stable point at $\phi = \pi$ to become unstable and gives rise to two new stable fixed points, which lie in the foci of the Cassini oval-shaped trajectories for the π-oscillations. For the special case $z_i = 0$, no new stable fixed points appear and all π-oscillations disappear, as shown in figure A.6.

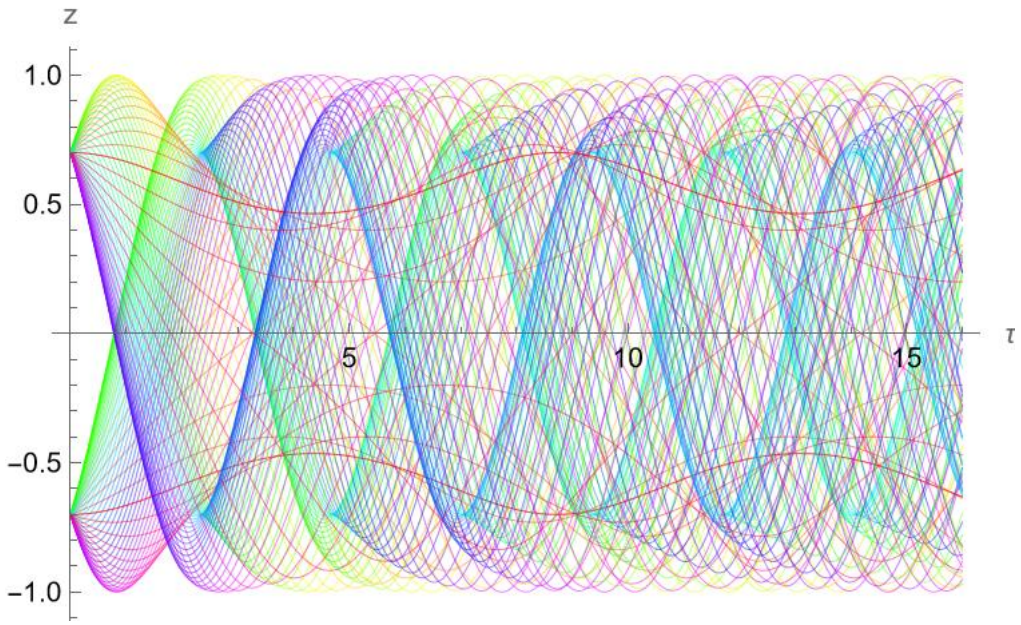

Figure A.5.: Mean-field trajectories in Fock space with $\bar{\Omega} = 0.5$, $\Lambda = 1.25$ and $z_i = \pm 0.7$, for many different intital phase differeces ϕ_i. Here, some π-oscillations (red lines) are self-trapped on their respective side of Fock space.

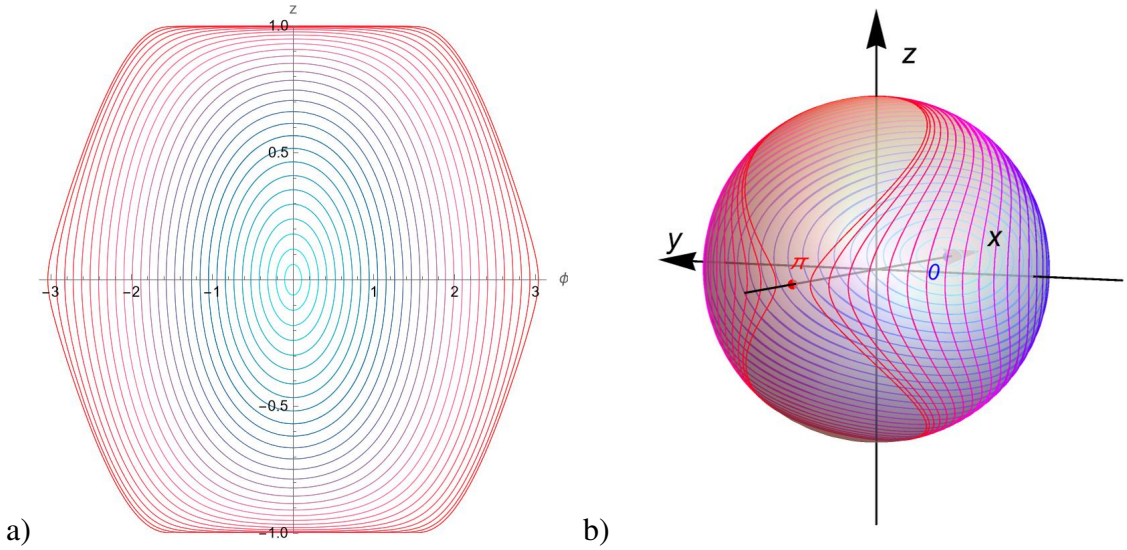

Figure A.6.: Mean-field phase space trajcetories with $\bar{\Omega} = 0.5$ (thus $\epsilon = 0$), $\Lambda = 2$ and $z_i = 0$. The many initial phase differences ϕ_i are donoted by the colors. Here, $\Lambda > 1$, thus, self-trapping should happen. However, for $z_i = 0$ no new stable fixed points occur and all π-oscillations vanish.

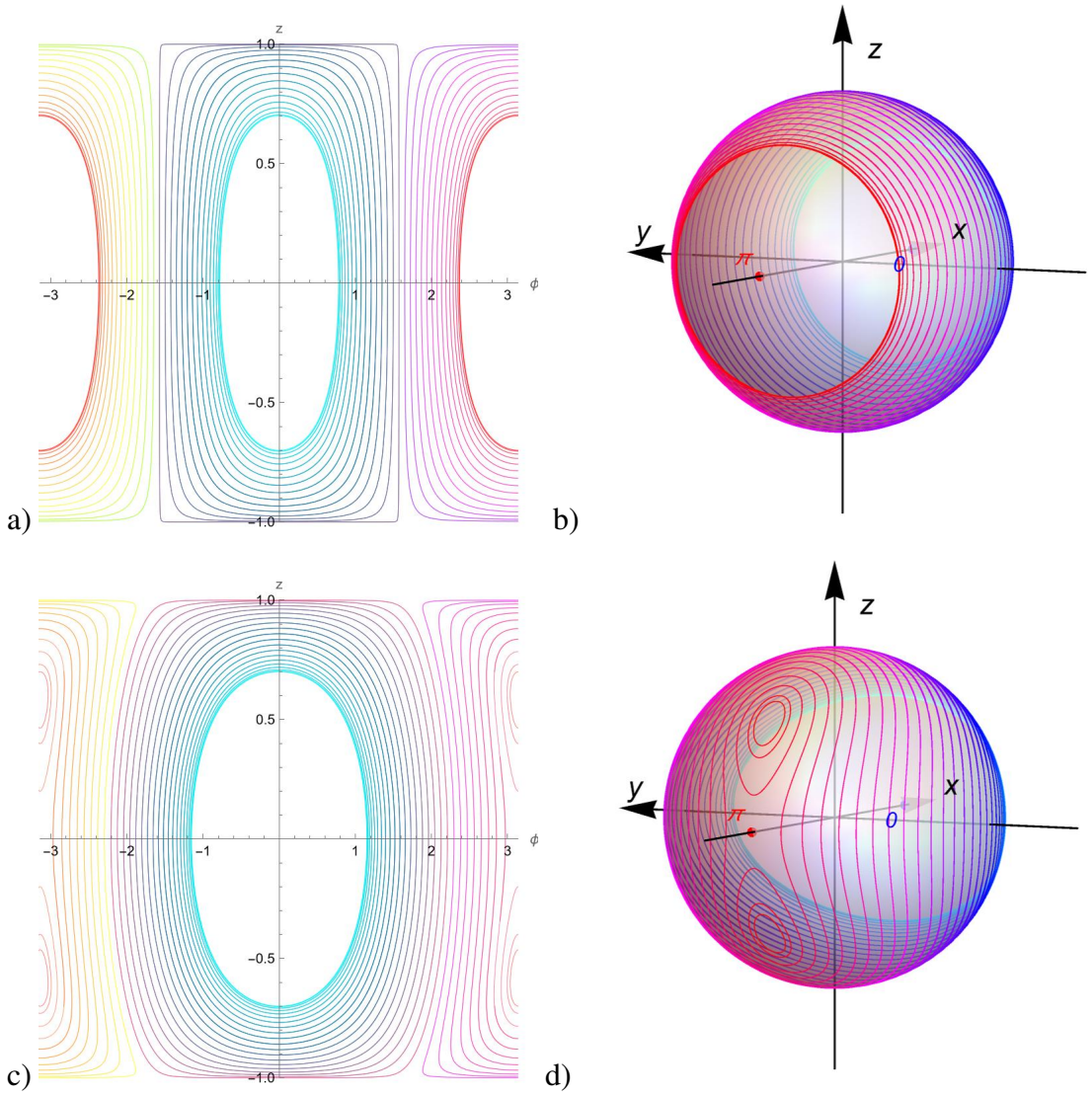

Figure A.7.: Mean-field phase space trajcetories derived from the Josephson equation (4.23, 4.24) with $\bar{\Omega} = 0.5$ (thus $\epsilon = 0$) and $z_i = \pm 0.7$. The many initial phase differences ϕ_i are donoted by the colors, where yellow and pink trajectories form the flat phase space (left) overalp in the Bloch sphere representation (right). Here, we tune the parameter Λ from $\Lambda \approx 0$ (upper row) past the critical values $\Lambda_c = 1$, for which the stationary point at $\phi = \pi$ becomes unstable, to $\Lambda = 1.25$ (lower row). This reproduces the essence of the bifurcation pictures 3.2 in the double-well system.

A.3. Quantum Trajectories and SPDM

A.3.1. SPDM Eigenvalues and Eigenvectors

When calculating the Fock space predictions from the SPDM, we combine the information from the time-dependent eigenvalues and eigenvectors. This is done as described in chapter 3.2.6 and presented here for completeness. Here, we present the eigenvalues over time and the evolution of probabilities per component in the eigenstates. For that, we plot $|a_\pm|^2$ and $|b_\pm|^2$ from equation 5.1 separately over time, we can see the time-evolution of the probability for the BEC to be in either of the two original modes. This gives us insight into what kind of linear combination of the two modes the eigenstate forms. Lastly, we also plot the eigenvectors as spinors on a sphere [28], with their trajectories over time. For this, we assume

$$\Psi_\pm = \cos(\theta_\pm/2)|0\rangle + e^{-i\Delta\Phi_\pm}\sin(\theta_\pm/2)|1\rangle, \tag{A.17}$$

where the global phase has been shifted to ensure the weight of the non-rotating state to be real, with $0 < \Delta\Phi_\pm < 2\pi$. Therefore, we can compare this to equation 5.1 and say $|a_\pm| = \cos(\theta_\pm/2)$ and $|b_\pm| = \sin(\theta_\pm/2)$, with the constraint $0 < \theta_\pm < \pi$ to ensure that $|a_\pm|$ and $|b_\pm|$ are always between 0 and 1. Now, we can find the angles for the spherical coordinates

$$\theta_\pm = 2\arctan\left(\frac{|b_\pm|}{|a_\pm|}\right) \tag{A.18}$$

$$\Delta\Phi_\pm = \arg(b_\pm). \tag{A.19}$$

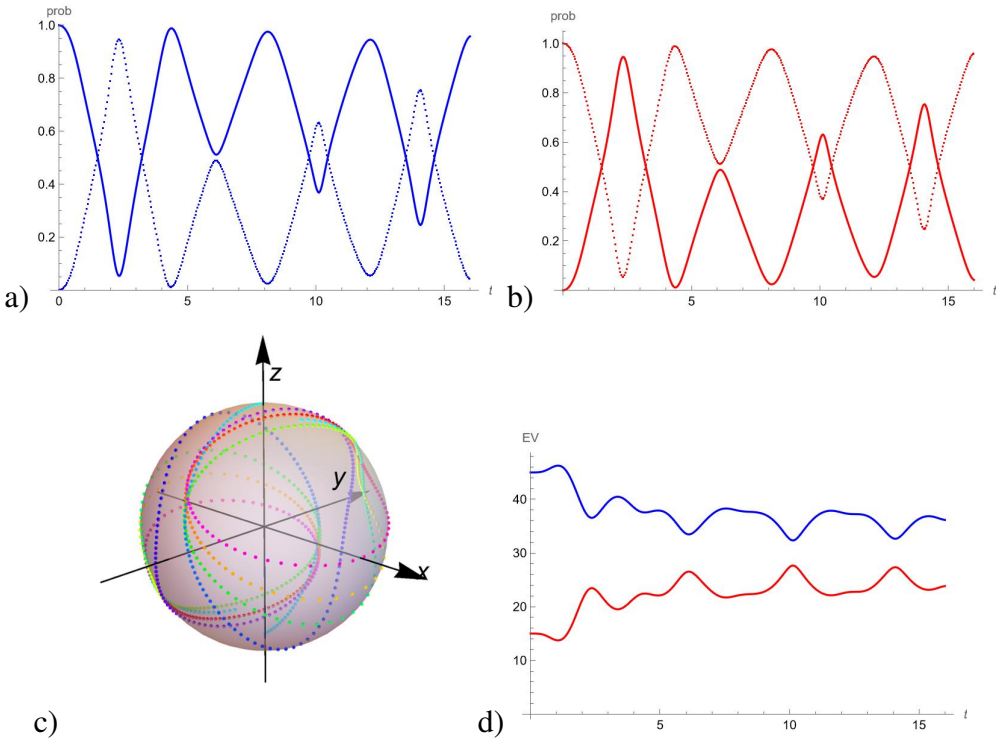

Figure A.8.: Eigensystem of SPDM when initial state is a Fock state with $N = 60$, $\Lambda = 2$, $\bar{\Omega} = 0.5$ (thus $\epsilon = 0$) and $z_i = 0.5$. For the eigenstates $\Psi_\pm = a_\pm|0\rangle + b_\pm|1\rangle$ we plot the evolution of $|a_\pm|^2$ (solid line) and $|b_\pm|^2$ (dashed line) over time separately in a) Ψ_+ and b) Ψ_-. In plot c) we show the eigenstates represented as spinors on a sphere according to equation A.17, where the different colors represent the time evolution. Plot d) shows the evolution of both eigenvalues over time, where the blue line belongs to the eigenstate Ψ_+ (plot a) and the red line to Ψ_- (plot b).

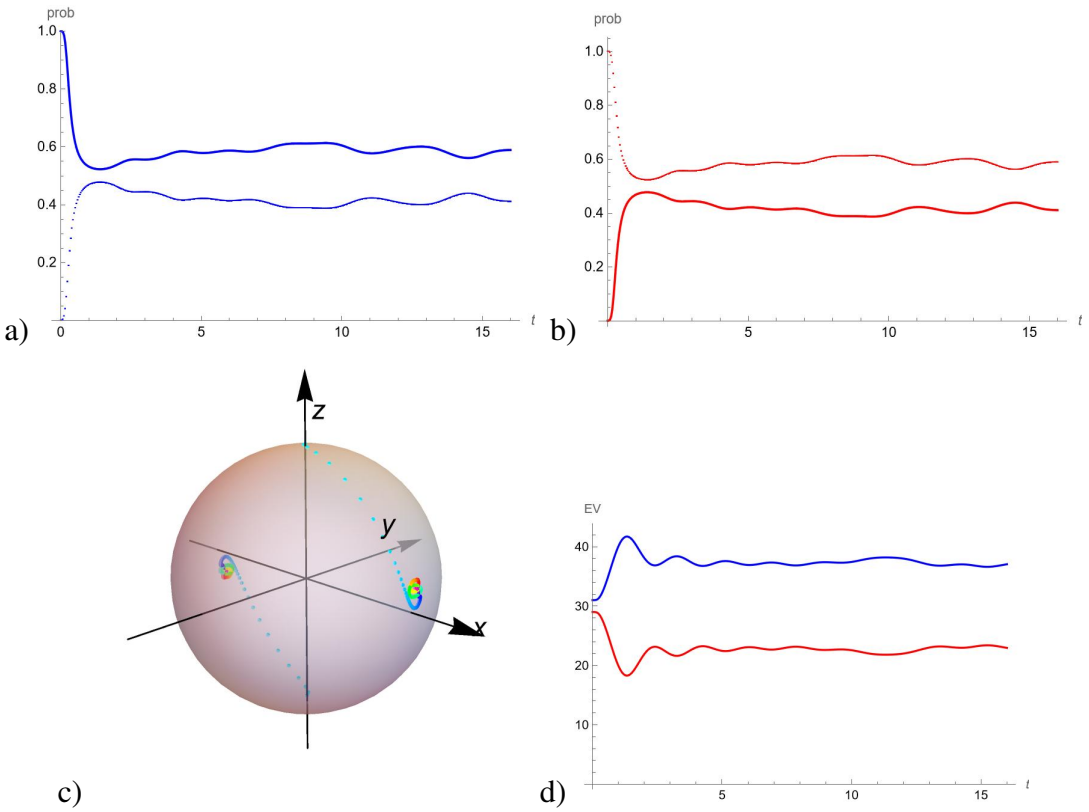

Figure A.9.: Eigensystem of SPDM when initial state is a Fock state with $N = 60$, $\Lambda = 2$, $\bar{\Omega} = 0.7$ (thus $\epsilon \neq 0$) and $z_i \approx 0$. For the eigenstates $\Psi_\pm = a_\pm|0\rangle + b_\pm|1\rangle$ we plot the evolution of $|a_\pm|^2$ (solid line) and $|b_\pm|^2$ (dashed line) over time separately in a) Ψ_+ and b) Ψ_-. In plot c) we show the eigenstates represented as spinors on a sphere according to equation A.17, where the different colors represent the time evolution. Plot d) shows the evolution of both eigenvalues over time, where the blue line belongs to the eigenstate Ψ_+ (plot a) and the red line to Ψ_- (plot b).

Fock state: full Overlap

When comparing the Fock state wavefunction to the classical trajectories, we reduced the number of trajectories and retained using the color code for the initial phases For completeness, we show their overlap in figure A.10. One can see, that they match pretty well, however, the plots are very busy. Therefore, we decided to reduce the colors in the main discussion.

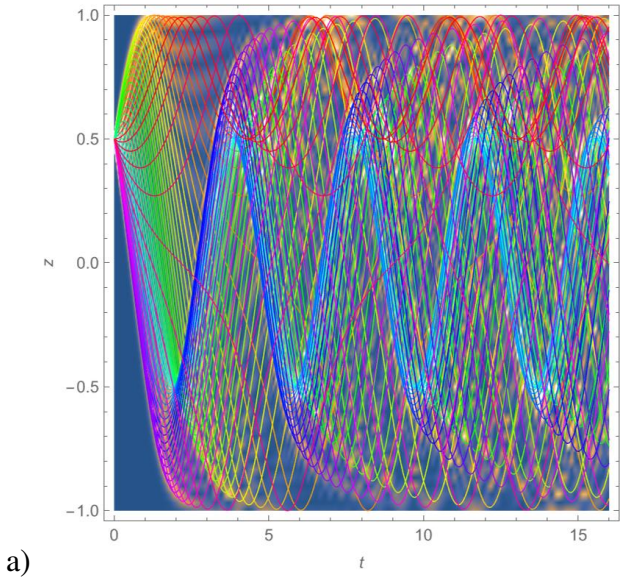

a)

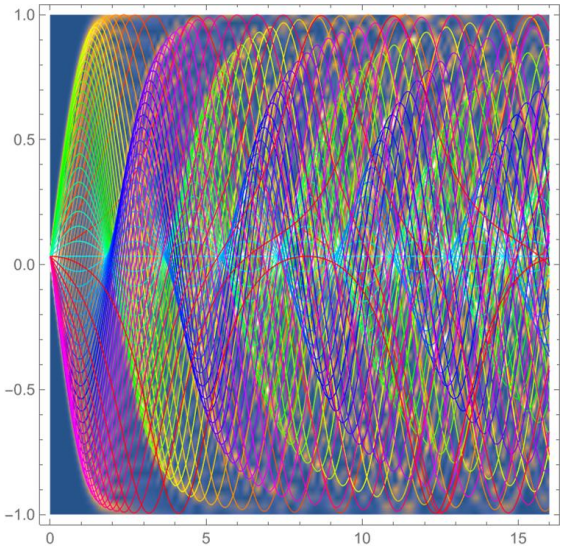

b)

Figure A.10.: Quantum trajectories in Fock space over time with $N = 60$, $\Lambda = 2$, compared to the classical trajectories from figure 5.4 a) with $z_i = 0.5$ and $\bar{\Omega} = 0.5$ (thus $\epsilon = 0$), and b) with $z_i \approx 0$ and $\bar{\Omega} = 0.7$ (thus $\epsilon \neq 0$).

A.3.2. Edge Fock State vs Coherent State

As mentioned in chapter 5.2, an extreme Fock state with $z \approx -1$ (all bosons in the rotating mode) is also considered an extreme coherent state with $\theta \approx 0$. Plotting the dynamics of the system for both these initial states gives insight into their similarities. Unfortunately, we cannot pick the exact extreme states in our code due to boundary issues. However, even for almost extreme states, we can already identify their similar behavior. The Fock state trajectories match better with the classical ones since they were achieved by using a pseudo-Fock state. Increasing the number of particles even further might allow us to get closer to the edge states, however, we already increased N compared to other plots to ensure better visualization. Here, the Fock state still splits into two branches, which would be combined for the actual extreme Fock state.

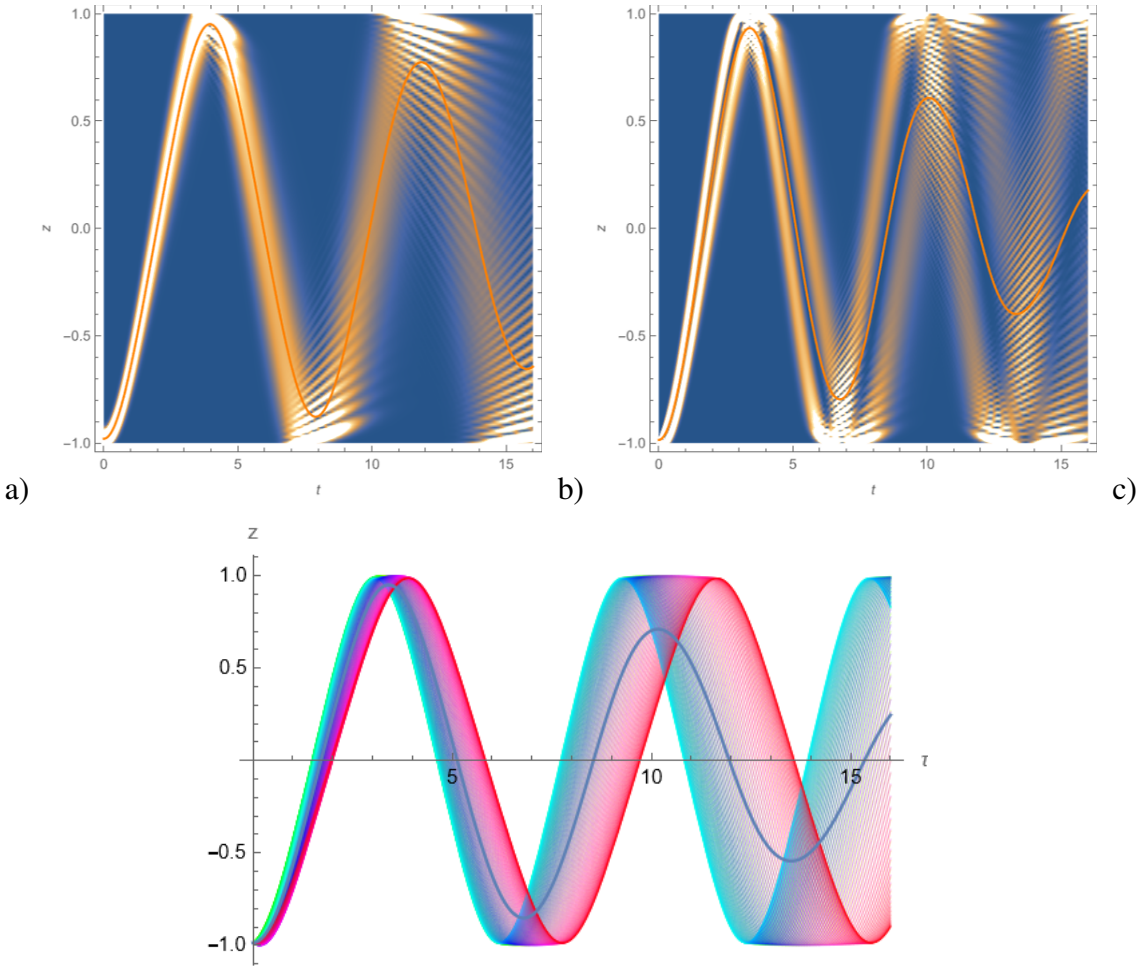

Figure A.11.: Quantum trajectories in Fock space over time with $N = 141$, $\Lambda = 1.1$,$\bar{\Omega} = 0.5$, for a) inital coherent state with $\theta \approx 0$, b) initial Fock state with $z \approx -1$, c) Pseudo-Fock state with classical trajectories.

A.3.3. Shifted Groundstate

As mentioned in chapter 5.2, the location of the ground state peak in Fock space depends on the value of $\bar{\Omega}_i$. However, since the choice is limited by the two-mode approximation. Therefore, no relevant shift can be made for a narrow ground state. Here, we present an example of a shifted ground state, with $\bar{\Omega}_i = 20$, which is far too large to be considered within this thesis. To make this visible, we also had to use $\Lambda_i = 500$, which is a factor 10 smaller compared to the narrow state presented before.

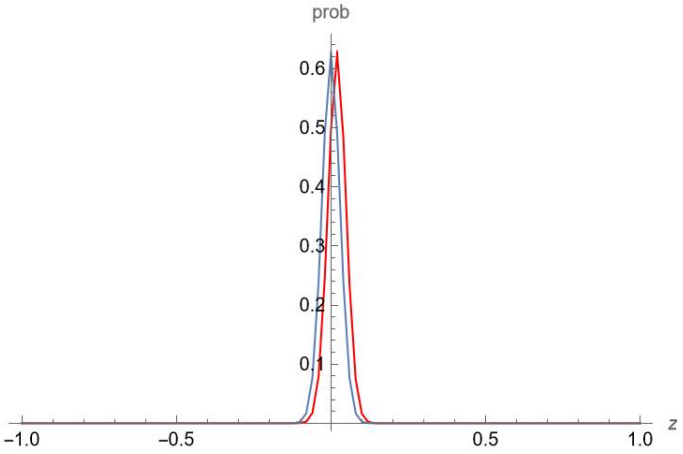

Figure A.12.: Groundstates in Fock space with $\bar{\Omega}_i = 20$, for $\Lambda_i = 500$.